

FOXMI expression reverts aging chromatin profiles through repression of the senescence-associated pioneer factor AP-1

Received: 9 June 2021

Accepted: 21 February 2025

Published online: 25 March 2025



Fábio J. Ferreira ^{1,2,3,4}, Mafalda Galhardo ^{1,2,3}, João M. Nogueira ^{1,2,5},
Joana Teixeira ^{1,2,5}, Elsa Logarinho ^{1,3} ✉ & José Bessa ^{1,2} ✉

Aging is characterized by changes in gene expression, some of which can drive deleterious cellular phenotypes and senescence. The transcriptional activation of senescence genes has been mainly attributed to epigenetic shifts, but the changes in chromatin accessibility and its underlying mechanisms remain largely elusive in natural aging. Here, we profiled chromatin accessibility in human dermal fibroblasts (HDFs) from individuals with ages ranging from neonatal to octogenarian. We found that AP-1 binding motifs are prevalent in elderly-specific accessible chromatin regions while neonatal-specific regions are highly enriched for TEAD binding motifs. We further show that *TEAD4* and *FOXMI* share a conserved transcriptional regulatory landscape controlled by a not previously described and age-dependent enhancer that loses accessibility with aging and whose deletion drives senescence. Finally, we demonstrate that *FOXMI* ectopic expression in elderly cells partially resets chromatin accessibility to a youthful state due to FOXMI's repressive function on several members of the AP-1 complex, which is known to trigger the senescence transcriptional program. These results place *FOXMI* at a top hierarchical level in chromatin remodeling required to prevent senescence.

Aging is characterized by the time-dependent functional decline that affects virtually all organisms. A relevant hallmark of such process is the progressive accumulation of senescent cells in many tissues¹. Cellular senescence, although historically seen as an irreversible cell-cycle arrest mechanism to prevent cancer, has gained solid evidence for its role in many biological processes like development, tissue repair, aging, and age-related diseases². According to several findings, senescence is actually a sequence of progressive and phenotypically different cellular states rather than a static terminus^{3,4}. Early senescent cells with activation of the p16^{INK4a} and/or p53–p21 pathways progress to full senescence by triggering extensive chromatin remodeling

underlying the production of a senescence-associated secretory phenotype (SASP).

Epigenetic changes play a key role during senescent cell evolution based on the discovery that partial reprogramming can modulate aging phenotypes in functionally compromised aged cells^{5,6}, and that epigenetic clocks are capable of estimating age accurately⁷. Epigenetic changes have been explored as part of the mechanisms controlling age-related transcriptional alterations, either by measuring the total load of histone modifications in human aging cells⁸ or by examining the genome-wide distribution of specific histone marks associated with transcriptional regulatory functions⁹. Moreover, remodeling of

¹i3S - Instituto de Investigação e Inovação em Saúde, Universidade do Porto, 4200-135 Porto, Portugal. ²Vertebrate Development and Regeneration Group, IBMC - Instituto de Biologia Molecular e Celular, Universidade do Porto, 4200-135 Porto, Portugal. ³Aging and Aneuploidy Group, IBMC - Instituto de Biologia Molecular e Celular, Universidade do Porto, 4200-135 Porto, Portugal. ⁴Graduate Program in Areas of Basic and Applied Biology (GABBA), Instituto de Ciências Biomédicas Abel Salazar (ICBAS), Universidade do Porto, 4050-313 Porto, Portugal. ⁵Doctoral program in Molecular and Cell Biology (MCbiology), Instituto de Ciências Biomédicas Abel Salazar (ICBAS), Universidade do Porto, 4050-313 Porto, Portugal. ✉e-mail: elsa.logarinho@i3s.up.pt; jose.bessa@ibmc.up.pt

the chromatin accessibility landscape has been reported in several cell and tissue types^{10–12}, with pioneer transcription factors (TFs) establishing accessible chromatin to which subsequent TFs can bind¹³. Furthermore, chromatin accessibility profiling in cellular models of oncogene-induced and replicative senescence has defined the dynamics and organizational principles of cis-regulatory elements (CREs) driving senescence transcriptional programs^{14,15}. One key player that imprints the senescence cis-regulatory signature is the activator protein 1 (AP-1) complex^{14–17}. Importantly, impairment of the pioneer TF JUN, a member of the AP-1 complex, partially reverts a transcriptional program of senescent cells¹⁴. These results suggest that increased AP-1 function leads to a senescent cellular state, although the mechanisms controlling AP-1 expression remain unknown.

Here, we investigated chromatin remodeling and TF redistribution in naturally aged human fibroblasts. We profiled age-related chromatin accessibility changes by performing Assay for Transposase-Accessible Chromatin using sequencing (ATAC-seq)¹⁸ in early passage human dermal fibroblasts (HDFs) retrieved from neonatal to octogenarian individuals. We found that elderly-specific accessible regions of the chromatin are enriched for AP-1 binding motifs, while neonatal-specific regions are enriched for binding motifs of TEAD TFs which, in complex with YAP/TAZ TFs, are key players of the Hippo signaling pathway regulating cell proliferation, stemness and differentiation¹⁹. We also found that changes in chromatin accessibility during aging correlate with transcriptional changes in regulatory landscapes. One example is the transcriptional regulatory landscape comprising *TEAD4* and *FOXMI*, which we found to be modulated by a not previously described enhancer whose accessibility is lost with aging. Excitingly, we demonstrated that FOXMI repressive function in the promoters of several members of the AP-1 complex is required to sustain chromatin accessibility at a youthful state. Thus, we bring mechanistic insight into FOXMI repression during natural aging and disclose its top hierarchical function in rescuing AP-1-driven senescence.

Results

Changes in chromatin accessibility during cellular aging are associated with enrichment of AP-1 binding motifs and loss of TEAD binding motifs

To understand the impact of natural aging in the accessibility of chromatin profiles in a genome-wide manner, we performed ATAC-seq in neonatal and elderly HDFs at early cell culture passage, with population doublings well below replicative exhaustion²⁰. We assessed peak reproducibility and differential accessibility (IDR and DESeq2; $\text{Log}_2\text{FC} > 1$, adjusted p -value < 0.05). We found 18377 sequences that are more accessible in neonatal cells (neonatal-specific), 39611 sequences more accessible in elderly cells (elderly-specific), and 74736 sequences without statistically different chromatin accessibility between neonatal and elderly cells (common; Fig. 1a–c; Supplementary Data 1). We intersected the ATAC-seq peaks with available ENCODE candidate cis-regulatory elements (cCREs)²¹ (Fig. 1d; Supplementary Data 2) and found that about 60% of peaks from both ages overlap with distal enhancer-like elements. In contrast, we found that the percentage of overlap with promoter-like and proximal enhancer-like elements is smaller in age-specific sequences than in common sequences (19% of common, 7% of neonatal-specific and 3% of elderly specific sequences overlap with promoter-like elements; 21% of common, 14% of neonatal-specific and 10% of elderly-specific sequences overlap with proximal enhancer-like elements; Supplementary Data 2). These data suggest that most age-associated changes in chromatin accessibility in HDFs occur in distal enhancer-like elements (62.8% of all ATAC-seq peaks in these datasets; Fig. 1d), which typically regulate multiple genes. Next, we performed a motif enrichment search for TF binding sites in neonatal- and elderly-specific open chromatin regions. We analyzed and compared the enrichment of

each TF motif in elderly- and neonatal-specific regions (Fig. 1e; Supplementary Data 3). We observed that binding motifs for TEAD proteins were less enriched in elderly-specific sequences ($\Delta\Delta$ enrichment: *TEAD3*: -8.2%; *TEAD1*: -7.7%; *TEAD4*: -6.3% and *TEAD2*: -4.8%), followed by binding motifs for AP-2 proteins (*TFAP2C*: -5.0%; *TFAP2A*: -4.6%), FOX proteins (*FOXFI*: -4.1%; *FOXMI*: -3.9%; *FOXO3*: -3.4%) and bHLH factors (*TWIST2*: -3.1%; *BHLHA15*: -3.1%; *TCF4*: -2.9%), while members of the AP-1 complex were more enriched in elderly-specific sequences ($\Delta\Delta$ enrichment: *JUN*: 13.0%; *ATF3*: 12.7%; *FOS*: 11.8%; and *JUNB*: 10.8%; Fig. 1e). Similar results were obtained when using an extended number of HDF samples ($N = 8$; age range: 1 day-old to 87 years-old) to compare the specific accessible regions in young individuals ($N = 4$; age range: 1 day-old to 10 years-old) vs. older individuals ($N = 4$; age range: 42 to 87 years old) (Supplementary Fig. 1a–e; Supplementary Data 1, 4). Noteworthy, these results suggest that both TEAD and FOX TFs exhibit inversely correlated dynamics with AP-1 TFs during aging. This is in agreement with previous studies reporting TEAD-mediated senescence inhibition by the Hippo pathway²², and senescence accrual by age-associated downregulation of FOXM1^{20,23} and FOXO3^{24,25}. Also, it is concurring with the reported enrichment of AP-1 binding motifs in open chromatin regions of induced senescent cells^{14,15} and murine aged cell types^{26,27}. Inversely correlated dynamics between TEAD (but not FOXM1) and AP-1 TFs were also found when we analyzed the ATAC-seq data from Martínez-Zamudio and colleagues using oncogene-induced senescent (OIS) WI-38 fibroblasts¹⁴ (Supplementary Fig. 1f–h; Supplementary Data 5). Binding motifs for TEAD proteins were less enriched ($\Delta\Delta$ enrichment: *TEAD3*: -13.9%; *TEAD1*: -13.8%; *TEAD4*: -11.5% and *TEAD2*: -8.0%) and binding motifs of members of the AP-1 complex were more enriched ($\Delta\Delta$ enrichment: *JUN*: 15.1%; *ATF3*: 14.6%; *FOS*: 13.4%; and *JUNB*: 12.8%) in senescent vs. control cells (Supplementary Fig. 1f–h; Supplementary Data 5). This suggests that the differences in the chromatin accessibility profile in naturally aged and induced senescent fibroblasts are partially conserved.

Changes in chromatin accessibility during aging correlate with transcriptional shifts in genomic landscapes

To evaluate the relevance of the chromatin state during aging, we correlated the accessibility of age-specific regions with the transcriptional output of nearby genes. We analyzed available transcriptomic datasets for HDFs retrieved from the same neonatal and elderly donors, cultured under the same conditions²⁰ and we established two sets of genes, either up or downregulated during aging. For each gene of the up or downregulated set, we quantified the number of neonatal-specific (closed with age) and elderly-specific (open with age) ATAC-seq peaks that are located in their genomic vicinity (from 20 kb to 100 kb). We observed that the number of neonatal-specific peaks is higher in the genomic landscapes of downregulated genes than in upregulated genes with aging (Fig. 1f). Conversely, the number of elderly-specific peaks is higher in the genomic landscapes of upregulated genes than in downregulated genes with aging (Fig. 1g). Importantly, in both comparisons, these differences became more striking when analyzing larger genomic landscapes, up to 100 kb centered in each gene (Fig. 1f, g). Noteworthy, the number of age-independent accessible peaks between genes that are up and downregulated during aging was not significantly different (Supplementary Fig. 1i). Altogether, these results suggest that genes whose expression changes with advancing age are under the control of CREs, which in turn are modulated by changes in chromatin accessibility during aging. Moreover, the difference in the average number of ATAC-seq peaks near up and downregulated genes increases with the extended span of the genomic landscapes (from 20 kb to 100 kb), both for neonatal and elderly-specific peaks, pointing to the existence of

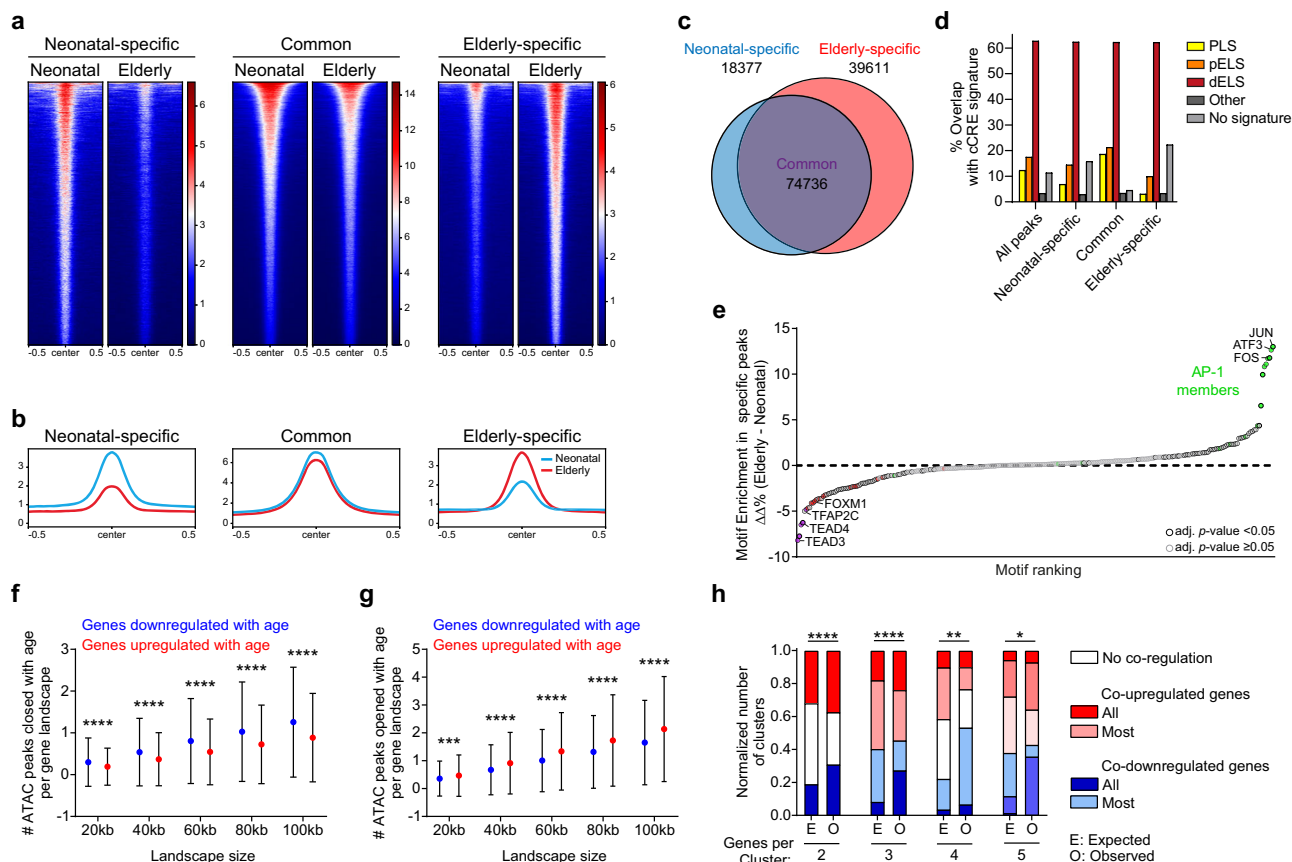


Fig. 1 | Chromatin accessibility variation during aging. **a** Heatmaps showing ATAC-seq signals across age-specific and common peaks in neonatal and octogenarian HDFs. Distance from center in kb. Y axis represents mean aligned reads per base from two biological replicates. **b** Profile plots of age-specific and common ATAC-seq peaks in neonatal and octogenarian HDFs. Distance from center in kb. Y axis represents mean aligned reads per base from two biological replicates, across all peaks. **c** Venn diagram showing overlap between neonatal- and elderly-specific ATAC-seq peaks and cCRE signatures defined from ENCODE data. PLS promoter-like signatures, pELS proximal enhancer-like signatures, dELS distal enhancer-like signatures, Other: DNase-H3K4me3 and CTCF-only signatures; No signature: no overlap with any mapped cCRE signature. **d** Relative quantification of overlap between each set of ATAC-seq peaks and cCRE signatures. **e** Comparison of HOMER-defined Known Motif Enrichment between elderly- and neonatal-specific ATAC-seq peaks. Colors highlight motifs of TEAD TFs (purple), FOX TFs (red), and AP-1 complex TFs (green). p -value determined using a two-tailed z -test, adjusted with Bonferroni–Dunn

correction. Motifs with adjusted p -value < 0.05 with a black border, motifs with adjusted p -value ≥ 0.05 with a gray border. Exact p -value and n for each motif reported in Supplementary Data 3. **f, g** Quantification of ATAC-seq peaks that close (**f**, neonatal-specific) or open (**g**, elderly-specific), in genomic landscapes of genes that are down- (blue) or upregulated (red), during aging. Values represent mean ± SD number of ATAC-seq peaks across 1435 downregulated genes and 1860 upregulated genes. ** p -value ≤ 0.01; **** p -value ≤ 0.0001 determined by a two-tailed Mann–Whitney U test. **h** Quantification of gene clusters, 2 to 5 genes per cluster, showing co-regulation (either up- or down-regulation) or no co-regulation of gene expression during aging. Among the 500 clusters found, 356 had 2 genes, 88 had 3 genes, 30 had 4 genes and 14 had 5 genes. The other 12 clusters had 6 or more genes (not shown). p -value was determined by χ^2 test between the expected (E) and observed (O) number of clusters per class. Source data are provided as a Source Data file.

large genomic landscapes where multiple genes are transcriptionally coordinated by common CREs during aging. To explore this hypothesis, we defined clusters of genes that are no more than 100 kb apart from each other and we asked if they presented a similar transcriptional change, either upregulation or downregulation during aging, in comparison to a theoretical assumption of no co-regulation. We observed that the gene clusters, regardless of their size (2 to 5 genes), exhibited coordinated transcriptional changes during aging (Fig. 1h; Supplementary Data 6), further supporting the existence of age-associated regulatory landscapes. Overall, we found 500 gene clusters containing 1268 out of 3295 (38.5%) differently expressed genes in aging HDFs (356 clusters with 2 genes, 88 clusters with 3 genes and 56 clusters with 4 or more genes). Examples are shown in Supplementary Fig. 1j, k: the cluster comprising the inflammation-related genes *MMP2*, *LPCAT2* and *CAPNS2*²⁸, all upregulated in elderly HDFs and containing a higher density of elderly-specific accessible regions than neonatal-specific; and the cluster comprising the cell growth-associated

genes *FENDRR*, *FOXF1* and *FOXLI*²⁸, all downregulated in elderly HDFs and containing a higher density of neonatal-specific accessible regions than elderly-specific.

TEAD4, FOXM1 and RHNO1 belong to an aging-associated regulatory landscape

To understand if the coordinated transcriptional changes of several genes within a regulatory landscape could be determinant for aging, we focused on the landscape containing *TEAD4*, a member of the *TEAD* gene family that encodes TFs whose binding motifs were the most enriched in neonatal-specific ATAC-seq peaks (Fig. 1e; Supplementary Data 3). *TEAD4* is known to regulate cell proliferation, tissue growth and apoptosis^{29,30} and its repression has been associated with senescence in human mesenchymal stem cells³¹. Within the same genomic landscape, we found *FOXM1*, a gene encoding a TF required for a wide spectrum of essential biological functions, including DNA damage repair and cell proliferation^{32,33}, and whose ectopic expression was shown to revert senescence phenotypes in in vitro and in vivo models

of premature and natural aging^{20,23}. Importantly, the *FOXMI* binding motif was enriched in neonatal-specific ATAC-seq peaks (Fig. 1e; Supplementary Data 3). Furthermore, in the close genomic vicinity of *FOXMI* we found *RHNO1*, which has been implicated in DNA replication stress response^{34–36}. *FOXMI* and *RHNO1* exist in a head-to-head orientation, sharing a bidirectional promoter³⁷, further supporting that genes within this landscape might share regulatory information. Moreover, except for *ITFG2*, all the genes within this putative regulatory landscape (*FKBP4*, *FOXMI*, *RHNO1*, *TULP3*, *TEAD4* and *TSPAN9*; no information for *NRIP2* and *TEX52*) were found downregulated in elderly cells (Supplementary Fig. 2a; Supplementary Data 7), suggesting that the co-expression of these genes might sustain a youthful cell fitness. Promoter DNA methylation was ruled out as the causal mechanism behind the aging-associated coordinated transcriptional downregulation of the *TEAD4/FOXMI/RHNO1* gene cluster since we found the *FOXMI/RHNO1* promoter to be hypomethylated in both neonatal and elderly HDFs (p -value = 0.964; Supplementary Fig. 2b). To assess co-regulation by shared CREs as an alternative mechanism, we pursued with a 4C-seq analysis of chromatin interactions within this gene cluster in neonatal HDFs. We selected the bidirectional promoter of *FOXMI/RHNO1*, roughly located in the middle of the gene cluster, as the viewpoint for the 4C-seq experiment. We found interactions of the *FOXMI/RHNO1* promoter with several genomic regions, including promoters of nearby genes, spanning approximately 300 kb (Supplementary Fig. 2c), thereby supporting transcriptional co-regulation of genes within this regulatory landscape by shared distal CREs.

Attesting its functional relevance, the *TEAD4/FOXMI/RHNO1* gene cluster is conserved in several vertebrate lineages, including distant Gnathostomata species (about 473 million years) (Supplementary Fig. 3a)^{38,39}. Non-vertebrate species such as lancelets also present the bidirectional promoter configuration of *FOXMI* and *RHNO1* (or *RHNO1*-like)^{38,40–42} (Supplementary Fig. 3b, c). Moreover, the tunicate *Ciona intestinalis* presents a bidirectional promoter co-regulating *FOXMI* and a CCNB1PI-like gene^{39,43}, whose E3 ubiquitin-protein ligase function is shared with the human 9-1-1 complex comprising *RHNO1*^{34,44} (Supplementary Fig. 3d). These data suggest this genomic organization dates back about 550 million years and it is functionally advantageous to all Chordata³⁸ (Supplementary Fig. 3e).

C10 is an age-dependent CRE that controls the expression of *TEAD4*, *FOXMI* and *RHNO1*

Using the ATAC-seq datasets described above, we found many accessible chromatin regions in the genomic landscape of *FOXMI* and *RHNO1* (Fig. 2a). The promoter regions of *FOXMI/RHNO1* and the nearby genes overlap with open chromatin regions, supporting active gene transcription in neonatal HDFs²⁰. Many accessible loci are localized in inter- and intragenic regions, pointing to the existence of functional non-coding CREs regulating gene expression within the landscape. We then crossed our datasets from neonatal HDFs (4C-seq and ATAC-seq) with ChIP-seq data for H3K27ac, H3K4me3 and transcription factor clusters (TF clusters) from multiple cell types from the ENCODE project^{45,46} to explore putative functions of the open chromatin regions interacting with the *FOXMI/RHNO1* promoter. This combined analysis allowed us to select 14 putative CREs, which we designated C1 through C14 (Fig. 2a; Supplementary Data 8). All selected putative CREs include at least one open chromatin region (ATAC-seq) and very low levels of the H3K4me3 mark, thus excluding likely promoter regions⁴⁷. We then performed luciferase reporter assays to test the enhancer activity of the 14 putative CREs in neonatal HDFs (Fig. 2b). We found regions C2, C5, C9 and C10 to induce significant luciferase activity in comparison to the control, thus indicating that the *FOXMI/RHNO1* promoter interacts with active enhancers in neonatal HDFs. To determine if these enhancers contribute to *FOXMI* expression in these cells, we performed CRISPR/Cas9-mediated genomic deletions (Fig. 2c; Supplementary Fig. 4a–c) of the regions C2, C5, C9

and C10, as well as of the region C8, the closest open chromatin region to the *FOXMI/RHNO1* promoter without enhancer activity. Deletion of enhancers C5, C9 and C10 significantly downregulated *FOXMI* expression in polyclonal populations of neonatal HDFs retrieved using a Fluorescence-activated Cell System (FACS) (Fig. 2d). As expected, deletion of the C8 region had no impact on gene expression. These results suggest that enhancers C5, C9 and C10 are required to sustain *FOXMI* expression in neonatal HDFs. To examine if changes in the interactome of *FOXMI/RHNO1* promoter account for the *FOXMI* downregulation previously observed along aging²⁰, we then performed 4C-seq in elderly HDFs (Supplementary Fig. 5a). We found the interactome of the *FOXMI/RHNO1* promoter to be kept similar in neonatal and elderly HDFs. Thus, conformational changes at the *FOXMI/RHNO1* regulatory landscape unlikely explain the transcriptional shift observed in elderly cells. In contrast, we found many ATAC-seq peaks to be specific to either neonatal or elderly cells (Supplementary Fig. 5b), suggesting that alterations in accessible chromatin may contribute to the age-associated transcriptional changes. Hence, we took a closer look on the ATAC-seq peaks of the enhancer regions C2, C5, C9 (Supplementary Fig. 5c–e) and C10 (Fig. 3a) to explore differences between neonatal and elderly HDFs. We found chromatin accessibility to be retained in enhancers C2, C5, and C9, but not in enhancer C10, in elderly HDFs. Enhancer C10 comprises two open chromatin regions in neonatal HDFs, one of which becomes closed in elderly HDFs (Fig. 3a). We designated the age-independent region as C10-P1 and the age-dependent region as C10-P2. We further explored the chromatin accessibility of C10-P2 in individuals with intermediate ages and found a progressive loss of chromatin accessibility with aging (Supplementary Fig. 6a). Moreover, interrogation of previously published data¹⁴ showed that while C10-P1 is not affected by oncogene-induced senescence in WI-38 fibroblasts, C10-P2 loses chromatin accessibility in senescent cells (Supplementary Fig. 6b). Next, we observed that the deletion of either C10-P1 or C10-P2 in neonatal HDFs resulted in significant downregulation of *FOXMI* (Fig. 3b), suggesting that both C10 regions are functionally required for proper gene expression. Similarly, both C10-P1 and C10-P2 deletions restrained *RHNO1* and *TEAD4* expression (Fig. 3c, d). Noteworthy, deletion of the age-dependent region C10-P2 in HDFs derived from 1 and 10-year-old individuals was also found to be required for proper *FOXMI*, *RHNO1* and *TEAD4* expression (Supplementary Fig. 6c–h). Also, supporting the specific effect of C10-P2 deletion within the regulatory landscape, we did not observe downregulation of other genes in chromosome 12 (Supplementary Fig. 6i–l). Overall, the results demonstrate that the age-dependent C10 enhancer coordinates the expression of *FOXMI*, *RHNO1*, and *TEAD4*.

C10 deletion is sufficient to trigger senescence in neonatal HDFs

Since C10-P2 accessibility is lost in naturally aged cells, we asked if the deletion of this region in young HDFs (neonatal, 1-year-old and 10-year-old) is sufficient to trigger senescence, through *TEAD4/FOXMI/RHNO1* gene cluster downregulation. As previously reported for *TEAD4*, *FOXMI* and *RHNO1* repressions^{20,33,34,44,48–52}, we found that CRISPR/Cas9-mediated deletion of C10-P2 induced a decreased percentage of cells staining positive for the Ki67 proliferation marker (Supplementary Fig. 7a, b), and an increased percentage of cells staining positive for 53BP1/p21, a combination of markers indicative of cell cycle arrest associated with DNA damage (Supplementary Fig. 7c–g). Further supporting that C10-P2 deletion drives senescence, we found an increased percentage of p16-positive cells (Fig. 3e, f; Supplementary Fig. 7h–j) and a higher activity of the lysosomal enzyme senescence-associated β -galactosidase (SA- β -gal) (Fig. 3g, h; Supplementary Fig. 7k–n) in C10-P2-deleted vs. control cell populations from neonatal to 10 years-old individuals. We additionally measured mitotic duration, which increases with aging due to *FOXMI* repression²⁰, finding that C10-P2 deletion leads to mitotic delay (Supplementary Fig. 7o).

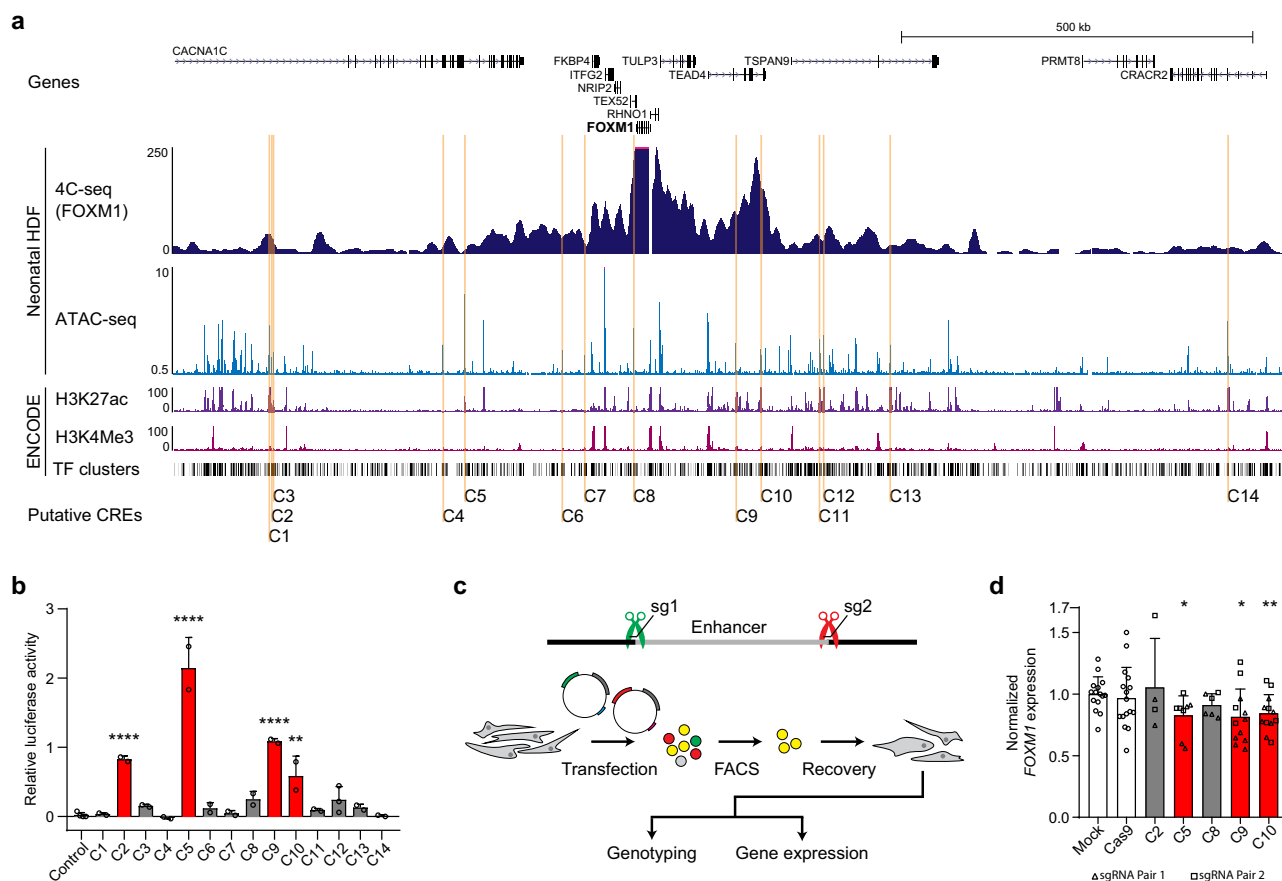


Fig. 2 | Non-coding genomic regions with enhancer activity are required for normal *FOXM1* expression. a Epigenetic features nearby *FOXM1/RHNO1*. 4C-seq data (dark blue) and ATAC-seq data (light blue) in neonatal HDFs. ChIP-seq data for H3K27ac (purple) and H3K4Me3 (pink), and TF clusters, all from the ENCODE project. Based on these attributes, 14 putative CREs (orange) were selected for further examination. **b** Luciferase reporter assay for the 14 putative CREs in neonatal HDFs. Red bars highlight sequences with significant enhancer activity. Each data point corresponds to a biological replicate equal to the mean of 3 technical replicates. Deletion of C2 ($n = 2$, p -value < 0.0001), C5 ($n = 2$, p -value < 0.0001), C9 ($n = 2$, p -value < 0.0001) or C10 ($n = 2$, p -value = 0.0038) significantly increase luciferase activity (red bars) compared to control ($n = 4$). ** p -value ≤ 0.01 ; **** p -value ≤ 0.0001 by one-way ANOVA with Dunnett's correction for multiple comparisons. Values represent mean \pm SD. **c** Experimental layout of CRISPR/Cas9-

mediated genomic deletions of putative *FOXM1* enhancers. **d** Gene expression analysis of *FOXM1* by RT-qPCR upon CRISPR/Cas9-mediated deletion of enhancers C2, C5, C9 and C10 and control region C8 in neonatal HDFs. Mock transfection and transfection with Cas9 alone (Cas9) were used as controls. Populations generated with sgRNA pair 1 or sgRNA pair 2 are distinguished by triangles and squares, respectively. Each symbol (circles, triangles and squares) corresponds to a biological replicate equal to the mean of three technical replicates. Deletion of C5 ($n = 8$, p -value = 0.0130), C9 ($n = 12$, p -value = 0.0146) or C10 ($n = 12$, p -value = 0.0098) significantly downregulates *FOXM1* (red bars) compared to mock ($n = 15$). * p -value ≤ 0.05 ; ** p -value ≤ 0.01 by two-tailed unpaired Student's t test. Values represent mean \pm SD. CREs, cis-regulatory elements. Source data are provided as a Source Data file.

Overall, the data demonstrate that CRISPR/Cas9-mediated deletion of C10-P2 induces a set of senescence-associated phenotypes in young HDFs, and suggest that the age-associated functional decline of an enhancer leads to a coordinated downregulation of (at least) three genes (*TEAD4*, *FOXM1* and *RHNO1*) whose knockdown has been associated to senescence.

***FOXM1* overexpression in elderly HDFs restores a youthful chromatin accessibility profile**

Among the co-regulated senescence-associated triad of genes - *TEAD4*, *FOXM1* and *RHNO1* - *FOXM1* stands out for its well-established role as modulator of aging phenotypes^{20,23}. We asked if this could be ascribed to a potential *FOXM1* function in chromatin remodeling. To test this, we ectopically expressed a constitutively active truncated form of *FOXM1* (*FOXM1-dNdKEN*)^{20,53,54} in elderly HDFs (Supplementary Fig. 8a, b) and performed ATAC-seq for chromatin profiling. We found that, after *FOXM1* ectopic expression, 25016 peaks became inaccessible (26.2% of all control peaks) and 14899 new accessible peaks were identified (17.5% of all peaks in elderly HDFs expressing *FOXM1*-

dNdKEN; Supplementary Fig. 8c). We then compared the peaks whose accessibility was altered by *FOXM1* overexpression with the neonatal-specific accessible peaks described above (Fig. 1c). We observed that 14840 out of the 25148 elderly-specific regions were closed (59.0%) and that, out of the 26334 neonatal-specific regions, 7042 were opened in elderly HDFs upon *FOXM1* overexpression (26.7%; Fig. 4a and Supplementary Fig. 8d; Supplementary Data 1). Conversely, 85.5% of the regions whose availability is kept during aging remain available upon *FOXM1* overexpression (60093 out of 70269; Supplementary Fig. 8d; Supplementary Data 1). These results suggest that the ectopic expression of *FOXM1* partially shifts the chromatin accessibility profile towards a youthful state. This shift is more evident in the number of closed chromatin regions (26.2% of all control elderly regions, 59.0% of elderly-specific regions) than in the number of opened regions (17.5% of all regions in *FOXM1*-overexpressing cells, 26.7% of neonatal-specific regions) in elderly HDFs as result of *FOXM1* overexpression, suggesting that *FOXM1* might predominantly repress factors that contribute to the establishment and maintenance of elderly-specific open chromatin regions. After performing motif discovery in elderly-specific

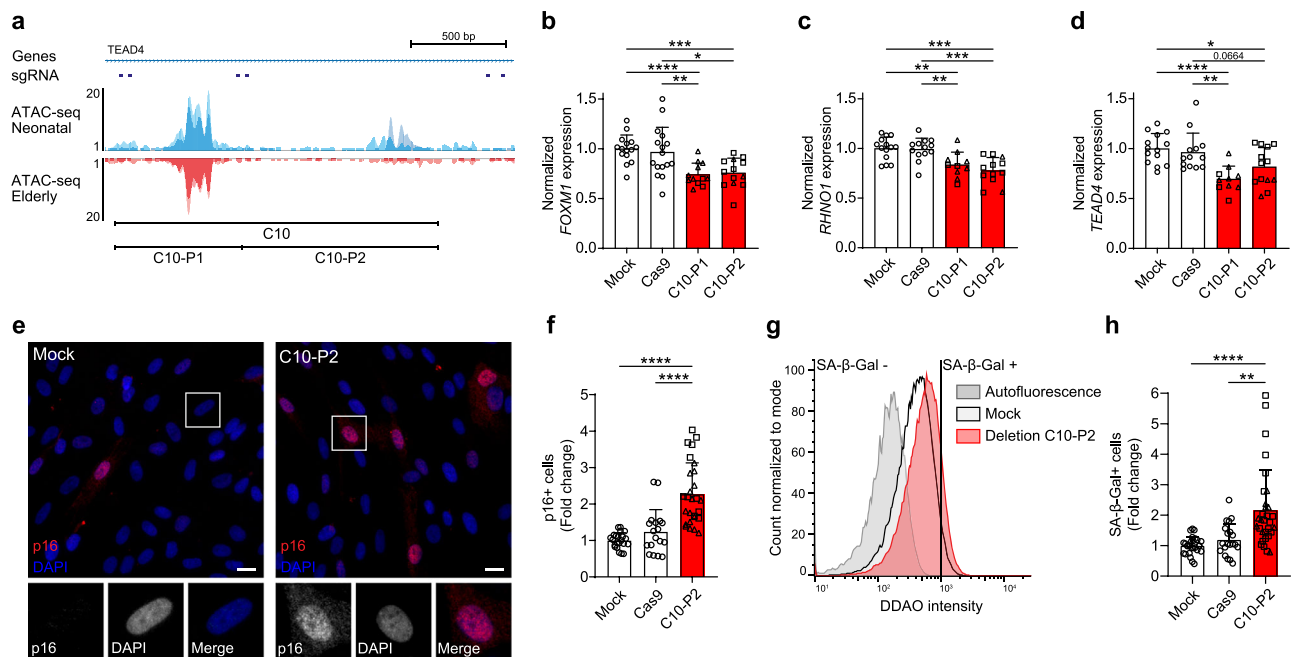


Fig. 3 | Deletion of enhancer with age-specific chromatin accessibility leads to gene expression changes and senescence phenotypes. a ATAC-seq profile of enhancer C10 in neonatal (blue) and octogenarian (red) HDFs. Different shades represent different individuals. Region C10-P1 is kept accessible while C10-P2 is closed in elderly cells. Dark blue squares represent regions targeted by sgRNAs. **b–d** Gene expression analysis of *FOXM1* (**b**), *RHO1* (**c**) and *TEAD4* (**d**) by RT-qPCR in neonatal HDFs carrying genomic deletion of C10-P1 or C10-P2 (red) compared to mock control cells and Cas9-only treated cells (white). Each data point corresponds to a biological replicate equal to the mean of 3 technical replicates. * p -value ≤ 0.05 ; ** p -value ≤ 0.01 ; *** p -value ≤ 0.001 ; **** p -value ≤ 0.0001 by two-tailed unpaired Student's t test. Values represent mean \pm SD. **e** p16/CDKN2A immunostaining (red) (DNA counterstaining with DAPI, blue) in mock-treated (left) and C10-P2-deleted (right) young HDFs. Insets highlight a p16-negative cell (left) and a p16-positive cell (right). Scale bar: 20 μ m. **f** Fold-change in the percentage of C10-P2-deleted cells staining positive for p16 (red) in young HDFs compared to mock-treated and Cas9-

only treated cells (white). Each data point represents a biological replicate (≥ 500 cells/replicate). **** p -value ≤ 0.0001 by two-tailed unpaired Student's t test. Values represent mean \pm SD. **g** Cytometry plot representing the frequency and intensity of SA- β -Gal activity in mock-treated cells (black outline) vs. C10-P2-deleted cells (red outline). A vertical line divides the intensities considered negative (SA- β -Gal-) and positive (SA- β -Gal+) for SA- β -Gal activity, based on the autofluorescence control (gray outline). **h** Fold-change in the number of cells positive for SA- β -Gal activity between mock-treated cells, Cas9-only treated cells and cells lacking C10-P2 (red), using young HDFs. Each data point represents a biological replicate ($\geq 30,000$ cells/replicate). ** p -value ≤ 0.01 ; **** p -value ≤ 0.0001 by two-tailed unpaired Student's t test. Values represent mean \pm SD. In all graphs (**b–d**, **f**, **h**), populations generated with sgRNA pair 1 or sgRNA pair 2 are distinguished by triangles and squares, respectively. Exact n and p -values provided in Source Data file. Source data are provided as a Source Data file.

regions that shift to an inaccessible state (closed) and in neonatal-specific regions that shift to an accessible state (opened) upon FOXM1 overexpression (Supplementary Fig. 8d), and comparing the motif enrichment in each dataset, we found that components of the AP-1 complex are less enriched in the opened peaks (*JUN*: -23.6%; *ATF3*: -23.6%; *FOS*: -21.9%), whereas CTCF (*CTCF*: 19.4%; *CTCF*: 18.4%) and bHLH motifs (*TWIST2*: 9.4%; *TCF4*: 9.2%; *BHLHA15*: 8.9%) are more enriched in the opened peaks (Fig. 4b; Supplementary Data 9). Since AP-1 is known to function as a pioneer factor on the remodeling of senescence-associated chromatin profiles^{14–17}, our results suggest that FOXM1 might downregulate members of the AP-1 complex.

FOXM1 is a repressor of the senescence-associated pioneer factor AP-1

We then explored if FOXM1 is a repressor of members of the AP-1 complex. The simpler mechanistic model would be FOXM1 operating via the promoter regions of components of the AP-1 complex. For this reason, we inspected the chromatin accessibility at the promoters of members of the AP-1 complex^{55,56}. We found the vast majority of these promoters to be accessible in both neonatal and elderly HDFs (Fig. 4c; Supplementary Data 10; Supplementary Fig. 8e), even though the expression of most AP-1 members increases with aging (Supplementary Data 10), concomitantly with reduced FOXM1 expression. Thus, we asked whether FOXM1 could control the expression of AP-1 members by acting, directly or indirectly, in their promoters. To this end, we cloned the promoter regions of the *JUN*, *ATF3* and *FOS* genes, encoding

AP-1 components previously associated with senescence^{14,15} and found upregulated in elderly cells²⁰, in luciferase reporter constructs. We transfected neonatal HDFs with these constructs and evaluated luciferase expression in response to FOXM1 knockdown by siRNA (siFOXM1). We found increased luciferase signal in siFOXM1 compared to controls, demonstrating that FOXM1 is indeed a repressor of AP-1 (Fig. 4d–f). In agreement with increased promoter activity, we found *JUN*, *ATF3* and *FOS* gene upregulation in siFOXM1 vs. control cells (Supplementary Fig. 8f–i). Moreover, analysis of previous RNA-seq data of elderly HDFs overexpressing FOXM1 and young HDFs treated with siFOXM1²⁰ further supported that FOXM1 modulates the transcriptional levels of AP-1 complex members (Supplementary Fig. 8j, Supplementary Data 11, 12). Overall, these results place FOXM1 as an upstream regulator of chromatin accessibility during aging and demonstrate that FOXM1 overexpression can act to revert age-associated chromatin profiles.

Discussion

Aging is characterized by temporal alterations of transcriptional profiles, many of which lead to a decline in cellular functions⁵⁷. These transcriptional changes have been suggested to be programmed⁵⁸. Transcriptional programs are controlled by chromatin accessibility, which remodels regulatory landscapes by altering the expression of gene clusters^{59,60}. Regulatory landscapes are characterized by many promoter-enhancer interactions allowing for gene cluster transcriptional coordination^{61,62}. Here, we showed that these same mechanistic

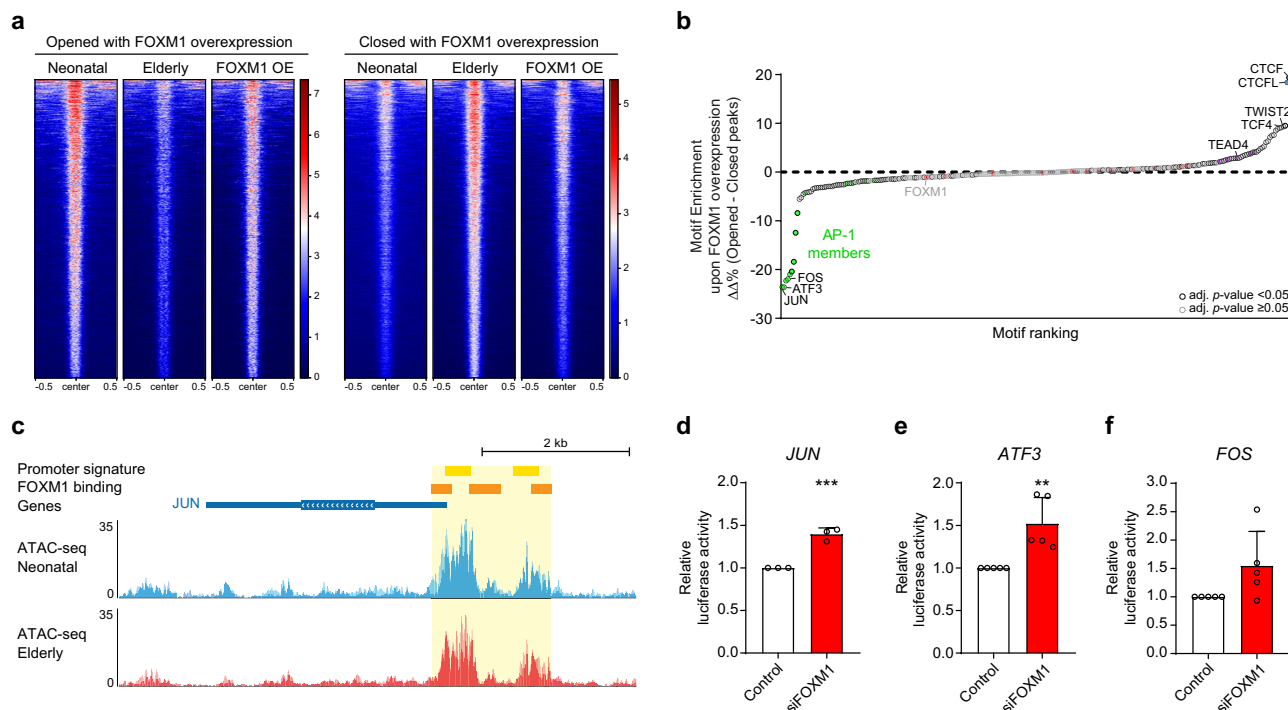


Fig. 4 | FOXM1 overexpression restores a youthful chromatin accessibility profile through repression of AP-1. a Heatmaps showing the ATAC-seq peak signals restored by FOXM1 in neonatal, elderly and FOXM1-overexpressing (FOXM1 OE) elderly HDFs. Signal is restored from the elderly profile to the neonatal profile by either increasing (chromatin opens, left) or decreasing (chromatin closes, right) upon lentivirus-mediated FOXM1 overexpression, in elderly HDFs. **b** Comparison of HOMER-defined Known Motif Enrichment between opened and closed ATAC-seq peaks upon FOXM1 OE. Positive values represent enrichment in opened peaks (present in neonatal but not in control elderly HDFs), while negative values represent enrichment in closed peaks (not present in neonatal HDFs but present in control elderly HDFs). Colors highlight motifs TEAD TFs (purple), FOX TFs (red), and AP-1 complex TFs (green). p -value determined using a two-tailed z -test, adjusted with Bonferroni-Dunn correction. Motifs with adjusted p -value < 0.05 with a black border, motifs with adjusted p -value ≥ 0.05 with a gray border. **c** Genomic

tracks representing epigenetic features in the *JUN* locus. Candidate cis-regulatory elements with promoter-like signature from the ENCODE project are shown in yellow. The region subsequently tested in promoter reporter assays is shown in light yellow. FOXM1 binding sites at *JUN* promoter defined by ChIP-seq data from the ENCODE project are shown in orange. ATAC-seq signal in neonatal (blue) and elderly (red) HDFs showing that chromatin accessibility is kept during aging. Different shades represent different individuals. **d–f** Gene expression analysis of *JUN* (**d**, Control $n = 3$, siRNA $n = 3$, p -value = 0.0007), *ATF3* (**e**, Control $n = 5$, siRNA $n = 5$, p -value = 0.0053) and *FOS* (**f**, Control $n = 5$, siRNA $n = 5$, p -value = 0.0768) by RT-qPCR in neonatal HDFs treated with siRNA against FOXM1. Each data point corresponds to a biological replicate equal to the mean of 3 technical replicates. ** p -value ≤ 0.01 ; *** p -value ≤ 0.0001 by two-tailed unpaired Student's t test. Values represent mean \pm SD. Source data are provided as a Source Data file.

principles apply to the aging transcriptional programs. We demonstrated that age-dependent closed and opened chromatin correlates with down- and upregulation of nearby genes' expression, respectively. These results highlight the potential that TFs and pioneer TFs might have dictating aging transcriptional programs, as previously suggested^{14–17,26}. We also disclosed that genes differentially expressed during aging tend to be clustered in the genome, exhibiting similar transcriptional changes. We further examined a specific regulatory landscape that contains key genes linked to aging: FOXM1 that is gradually repressed along advancing age, driving aging phenotypes^{20,23}; and TEAD4, a member of the YAP/TAZ-TEAD pathway, whose activity and nuclear localization declines in old dermal fibroblasts⁶³, and whose downregulation drives senescence^{22,31}. Conversely, FOXM1 and YAP sustained expressions are able to delay senescence and its associated traits in animal models of physiological and accelerated aging^{23,31,63}. Interestingly, YAP-TEAD physically interacts with the MMB-FOXM1 complex to promote the expression of late cell cycle genes through long-range interactions on chromatin between YAP-TEAD mainly at enhancers and MMB-FOXM1 mainly at promoters^{64,65}. In our study, we found that binding motifs for both FOXM1 and TEAD4 were enriched in neonatal-specific available chromatin regions. We showed that this regulatory landscape comprises up to 9 genes and is partially conserved in vertebrate genomes. We demonstrated that at least TEAD4, FOXM1, and RHNO1 are co-regulated by an enhancer that is active in

neonatal HDFs and inactive in elderly HDFs. Within this regulatory landscape, other genes (e.g. FKBP4, TULP3 and TSPAN9) were slightly downregulated with aging, except ITFG2, which was marginally upregulated in elderly HDFs. Interestingly, ITFG2 is a component of the KICSTOR complex which, under catabolic conditions, functions as a negative regulator in the amino acid-sensing branch of mTORC1, known to be activated in aging⁶⁶. FKBP4 is among the top-5 genes most consistently downregulated with age across datasets for key mammalian tissues⁶⁷, and TULP3 mutations cause multisystem fibrosis originating from disrupted ciliary composition and DNA damage⁶⁸. Altogether, this highlights the functional role of the regulatory landscape in aging processes.

By studying chromatin conformation and accessibility in the genomic landscape of TEAD4 and FOXM1, we found a not previously described enhancer (C10) containing an age-dependent accessible region, named C10-P2, that interacts with the FOXM1/RHNO1 promoter. We showed this region to be required for proper expression of FOXM1, RHNO1 and TEAD4, and its deletion to induce senescence in neonatal HDFs. Although our data indicated that FOXM1 expression is modulated by multiple accessible loci with enhancer activity in neonatal HDFs, and even though reorganization of topological domains has been associated with in vitro senescence^{69–71}, we found the interactome at the FOXM1/RHNO1 promoter to be largely stable with aging. In contrast, we found many regions with age-dependent

accessibility states, in line with previous reports using other cell types and in vitro senescence^{14,15,26,72–75}. Notably, while the chromatin accessibility of the *FOXMI/RHNO1* promoter and most *FOXMI* enhancers is maintained in elderly HDFs, the enhancer region C10-P2 becomes inaccessible. Interestingly, the genes co-regulated by the C10 enhancer, *FOXMI*, *RHNO1* and *TEAD4*, have all been associated with cell proliferation^{34,37,49–51}, DNA damage response^{33,34,44,52} and senescence^{4,20,22,31}. Although the downregulation of *FOXMI*, *RHNO1* and *TEAD4* upon the deletion of C10 is moderate, likely due to the contribution of other enhancers such as C5 and C9 (Fig. 2b, d), it is sufficient to trigger an increase of senescence markers. Therefore, our findings demonstrate the pivotal importance of the C10 enhancer in the regulation of a transcriptional hub required for cell homeostasis and survival, suggesting that changes in a single, master cis-regulatory element contribute to the transcriptional drift towards senescence. Although future studies are needed to dissect the molecular mechanisms controlling C10 availability, the uncovered properties of C10 open perspectives to ameliorate aging features by modulating the activity of this enhancer using targeted site-directed approaches^{76,77}.

Most strikingly, we found that chromatin regions that are specifically available in neonatal and young HDFs are enriched for binding motifs of TEAD TFs and FOX TFs, such as *FOXMI* and *FOXO3*, for which genetic polymorphisms and upregulation have exhibited consistent associations with increased human longevity⁷⁸. Other factors, such as AP-2 and bHLH factors, are also enriched in young-specific chromatin regions, likely embodying their roles in stimulation of the Hippo pathway^{79,80} and repression of proinflammatory cytokines⁸¹, and in dermal maturation and function^{82,83}, respectively. Distinctly, we found that elderly-specific available regions exhibit prevalent binding motifs of the AP-1 complex. These results are concurring with previous studies in induced senescence models, in which AP-1 TFs have been described as pioneer factors that bind and remodel chromatin, thus triggering and maintaining a reversible senescence transcriptional program^{14,15}. Similarly, recent studies suggest that AP-1-mediated chromatin opening is associated with normative aging, particularly across multiple murine tissues^{26,27,84}. In this work, we show that the expression of genes from the AP-1 complex is repressed by *FOXMI*, a gene highly expressed in neonatal cells and that is transcriptionally downregulated along age. This conclusion is supported by multiple lines of evidence. First, upon *FOXMI* overexpression in elderly HDFs, we observed that more genomic regions closed than opened, suggesting that *FOXMI* represses factors that open chromatin during aging, a role that has been described for the AP-1 complex. Secondly, those closed regions are notably enriched for motifs of the AP-1 complex. Thirdly, *FOXMI* overexpression in elderly HDFs leads to transcriptional downregulation of AP-1 components, while *FOXMI* knockdown in young HDFs leads to upregulation of AP-1 components. Finally, using reporter assays, *FOXMI* knockdown increased promoter activity of some members of the AP-1 complex. Altogether, the results indicate that *FOXMI* acts as a repressor of the AP-1 complex in HDFs, although further studies will be required to determine if *FOXMI* controls AP-1 complex expression directly or indirectly, or if *FOXMI* also controls other factors regulating chromatin accessibility with age. These findings bring insight into AP-1 complex regulation during aging, with *FOXMI* repression accounting for the AP-1-driven senescence program. Indeed, we have previously shown the ectopic expression of *FOXMI* to revert senescence in vitro and in vivo^{20,23}. Here, we further unveil that ectopic expression of *FOXMI* acts to remodel the chromatin profile of elderly HDFs towards a youthful state. This epigenetic shift is supported by the similar enrichment in TEAD and bHLH TFs in the chromatin regions opened upon *FOXMI* overexpression (Fig. 4b), and across neonatal- and young-specific open chromatin regions (Fig. 1e and Supplementary Fig. 1e). Moreover, the enrichment in CTCF motifs upon *FOXMI* overexpression may reflect the rescue of CTCF age-

related transcriptional downregulation⁸⁵ and reorganization of its senescence-associated chromatin binding⁷⁰. Our findings suggest that these chromatin changes are induced indirectly through the repression of the AP-1 complex. This is in agreement with the reported reversion of senescence transcriptional programs upon AP-1 knockdown^{14,15}. Importantly, the promoters of *JUN*, *ATF3* and *FOS*, the three members of the AP-1 complex we examined, are accessible in both neonatal and elderly HDFs, and are thus potentially responsive to *FOXMI*-mediated repression in an age-independent manner. These observations highlight the potential usage of AP-1 negative regulators, such as *FOXMI*, to revert senescence-associated phenotypes in elderly cells, as we have shown by ectopically expressing *FOXMI*. Importantly, these results also suggest that the AP-1 complex is required not only to trigger but also to maintain elderly-specific chromatin profiles and the senescence transcriptional program.

This study shows that young and older HDFs have significantly different chromatin accessibility profiles. Future studies should include a bigger sample size to better account for biological heterogeneity and individuals that gradually span the lifetime to investigate if linear or nonlinear (age-specific waves)⁸⁶ changes in chromatin accessibility account for an evolving epigenetic senescence state. Furthermore, such profiling could help to disentangle chromatin states related to development from those exclusively associated with aging. Interestingly, many of these states might be inherently entangled, as the cis-regulatory transition from cell maturation to aging appears to evolve as a continuum rather than abrupt shifts²⁶ and senescence-associated transcriptional profiles are progressive and asynchronous⁸⁷.

Relevantly, this study advances our understanding of the *FOXMI* key role in aging, strengthening its senotherapeutic potential. We identified a cis-regulatory element whose accessibility is lost during aging and that accounts for *FOXMI* downregulation, as well as for the downregulation of other genes within the regulatory landscape that, altogether, represents a crucial transcriptional hub required to sustain cell fitness and to prevent senescence. In addition to this regulatory landscape, the study further discloses *FOXMI* as a repressor of pioneer factors of the AP-1 family, driving (and maintaining) a senescence transcriptional program, and as being able to significantly rescue the changes in chromatin accessibility that account for genome-wide altered regulatory landscapes in aging. Noteworthy, *FOXMI* induction does not appear to change indiscriminately the chromatin profile of elderly cells, but rather to mainly revert age-specific regions. This grades *FOXMI* induction as a safe strategy capable of reprogramming an aging transcriptional program and of reverting aging phenotypes.

Methods

Cell culture

Human fibroblasts established from skin biopsies of healthy Caucasian males were acquired from ZenBio (Neonatal, DFM021711A) and NIGMS Human Genetic Cell Repository, Coriell Institute (Neonatal, GM21811; 1y, GM05659; 10y, GM03348, GM09503; 42y, AG06235; 52y, GM23667; 75y, AG11073; 87y, AG10884). Only early passage dividing fibroblasts were used in all experiments. Cells were cultured in Minimal Essential Medium (MEM) with Earle's salts and L-glutamine (10-010-CV, Corning) supplemented with 15% Fetal Bovine Serum (Gibco) and 1× Antibiotic-Antimycotic (Gibco) in ventilated flasks at 37 °C and humidified atmosphere with 5% CO₂. Cells were maintained so that confluency was always below 90%.

Viral Infection

Lentiviruses were produced using the Lenti-X Tet-ON Advanced Inducible Expression System (Clontech), following the protocol described therein. Briefly, HEK293T cells were transfected with packaging plasmids pMD2.G (Addgene #12259) and psPAX2 (Addgene #12260), along with transfer vectors, using Lipofectamine 2000 (Life

Technologies, Thermo Scientific, CA, USA). This resulted in the production of lentiviruses carrying either empty pLVX-Tight-Puro (Clontech) or pLVX-Tight-Puro-FoxM1-dNdK²⁰, as well as lentiviruses carrying pLVX-Tet-On Advanced (which expresses rtTA; Clontech). Fibroblasts were co-infected for 5–6 h with empty pLVX-Tight-Puro or FoxM1-dNdK- and rtTA-expressing lentiviruses at 2:1 ratio, in the presence of 8 µg/ml polybrene (AL-118, Sigma-Aldrich, MO, USA). After that time, fresh media with 750 ng/ml doxycycline (D9891, Sigma-Aldrich, MO, USA) was added to the cells to induce co-transduction. Phenotypes were subsequently analyzed and quantified 68 h after doxycycline treatment. Transfection efficiency was monitored by western blotting.

Western blotting

Lentiviral-infected elderly HDFs were detached with Trypsin, washed thrice with ice-cold PBS and lysed in lysis buffer (150 mM NaCl, 10 mM Tris-HCl pH 7.4, 1 mM EDTA, 1 mM EGTA, 0.5% IGEPAL) with 1x cOmplete, EDTA-free Protease Inhibitor (Roche). Lysates were quantified for protein content by the Lowry Method (DC™ Protein Assay, Bio-Rad, CA, USA). Twenty micrograms of total extract were loaded in SDS-polyacrylamide gels for electrophoresis and transferred onto nitrocellulose membranes for western blot analysis. Membranes were blocked during 1 h with TBS (50 mM Tris-HCl, 150 mM NaCl) containing 5% low-fat milk. Primary antibodies were diluted in TBS containing 2% low-fat milk: rabbit anti-FoxM1 (13147, ProteinTech Group, Inc.), 1:1000, and mouse anti-α-tubulin (T5168, Sigma-Aldrich, CA, USA), 1:50000. Horseradish peroxidase-conjugated secondary antibodies goat anti-rabbit (SC-2004, Santa Cruz Biotechnology) and goat anti-mouse (SC-2005, Santa Cruz Biotechnology) were diluted at 1:3000 in TBS containing 2% low-fat milk. Detection was done using Clarity Western ECL Substrate reagent (Bio-Rad Laboratories, CA, USA) as per the manufacturer's instructions. Quantitative analysis of protein levels was carried out using a GS-800 calibrated densitometer with Image Lab software (v6.0.1) (Bio-Rad Laboratories). Only the levels of endogenous full-length FOXM1 were quantified (note that FOXM1 binds its own promoter, therefore ectopic FOXM1-dNdKEN induces endogenous FOXM1).

Bisulfite sequencing

DNA samples were collected from cell cultures using the Quick-DNA Miniprep Plus Kit (Zymo Research) and promptly used for bisulfite DNA conversion. The EpiTect Bisulphite Kit (QIAGEN) was used according to the manufacturer's instructions. The *FOXM1/RHNO1* promoter region was amplified with iMax-II DNA Polymerase (INTRON) and the products cloned into the pCR8/GW/TOPO vector (Invitrogen). Primers used are listed in Supplementary Table 1. Clones were sequenced with Sanger sequencing. Sequencing data was analyzed, and the *p*-value determined with QUMA⁸⁸.

ATAC-seq (Assay for Transposase-Accessible Chromatin using sequencing)

ATAC-seq was performed on 50000 cells according to Buenrostro and colleagues⁸⁹ with minor modifications. Briefly, cells were detached with Trypsin, washed with ice-cold PBS, lysed in ice-cold fresh lysis buffer (10 mM Tris-HCl, pH7.5; 10 mM NaCl; 3 mM MgCl₂; 0.1% IGEPAL) and immediately incubated with homemade Tn5 transposase in TAPS-DMF buffer⁹⁰ at 37 °C for 30 min, followed by proteinase K treatment. Immediately after transposition the samples were purified with MinElute PCR Purification Kit (QIAGEN). We performed qPCR analysis on the samples to determine the appropriate number of PCR cycles to create the library, using 1 µL of tagmented DNA, 0.6 µL of 25 µM Ad Primer 1, 0.6 µL of 25 µM Ad Primer 2 (from 2.1 onwards), used for multiplexing, 1 µL 10x SYBR Green I (ThermoFisher Scientific), 5 µL KAPA HiFi HotStart ReadyMix (KAPA Biosystems) and 1.8 µL H₂O HyPure, with the program: 98 °C for 45 s; 72 °C for 5 min; 98 °C for 30 s; followed by 30

cycles of 98 °C for 10 s, 63 °C for 30 s, 72 °C for 30 sec. The final library was generated using 18 µL of tagmented DNA, 2.5 µL of 25 µM Ad Primer 1, 2.5 µL of 25 µM Ad Primer 2, 25 µL KAPA HiFi HotStart ReadyMix (KAPA Biosystems) and 2 µL H₂O HyPure, with the program: 98 °C for 45 s; 72 °C for 5 min; 98 °C for 30 s; followed by *N* cycles of 98 °C for 10 s, 63 °C for 30 s, 72 °C for 30 s; and 72 °C for 1 min. *N* is the number of cycles corresponding to one third of the maximum fluorescence intensity detected in the pilot qPCR. Primers used in this study are listed in Supplementary Table 1. The library was immediately purified using the QIAquick PCR Purification Kit (QIAGEN) and eluted in 20 µL. Successful tagmentation was confirmed with a TAE agarose gel electrophoresis.

Libraries were sequenced on a HiSeq 2500 system, High-Output mode, 2 × 100 bp paired-end, or NovaSeqX system, 2 × 150 bp paired-end, at Macrogen, South Korea. Analysis of raw reads quality and removal of sequencing adapters of each sample was done with FASTQC (v.0.11.8)⁹¹ and Skewer (v.0.2.1)⁹², respectively, or simultaneously with fastp (v0.23.2)⁹³. Reads were mapped to the reference human genome (GRCh38/hg38) using Bowtie2 (v.2.4.2 or higher)⁹⁴ with parameters “-X 2000 and --very-sensitive”. To avoid clonal artefacts, the duplicated mapped reads were removed using Samtools (v1.11)⁹⁵. Mapped reads were filtered by the fragment size (≤120 bp) and mapping quality (≥10) with a custom Python (v.3.7.2 or higher) script. To call for enriched regions, MACS2 (v.2.2.7)⁹⁶ with the parameters “--nomodel, --keep-dup 1, --llocal 10000, --extsize 74, --shift - 37 and -p 0.07” was used. ATAC-seq data from biological replicates were initially processed independently. Then, we applied the Irreproducible Discovery Rate (IDR) (v.2.0.3 or higher) to obtain a confident and reproducible set of peaks based on two replicates⁹⁷. Further analysis was performed with the ATAC-seq peaks with IDR score above 831 (reflecting a *p*-value < 0.01). To identify the open chromatin regions, the reproducible peaks were filtered to remove blacklisted regions⁹⁸, using BEDTools (v.2.29.2) intersect with default parameters⁹⁹. BEDTools intersect and merge were used to identify sample-exclusive peaks (such as Neonatal-exclusive, Elderly-exclusive or FOXM1 OE-exclusive) and peaks shared between samples (such as shared between Neonatal and Elderly). Differential accessibility analysis of shared peaks was performed with DESeq2 (v.1.32)¹⁰⁰, with differences considered statistically significant when adjusted *p*-value < 0.05 and log₂FC > 1. The differently accessible shared regions were combined with the sample-exclusive peaks for downstream analysis (resulting in datasets such as Neonatal-specific). The shared peaks with no differential accessibility enrichment were termed Common. The resulting BED files were deposited in the European Nucleotide Archive (ENA) and are described in Supplementary Data 1 and the Reporting Summary. Motif enrichment analysis was performed with HOMER (v.4.11)¹⁰¹, using findMotifsGenome.pl, with default parameters. To determine known motif enrichment for each sample, the difference between the percentage of sequences with the motif and the percentage of background sequences with the motif was calculated. Different enrichments in different samples were then compared by subtracting the enrichment in one sample by the other and ranking the motifs by size of enrichment. Thus, negative values represent enrichment in one sample-specific peaks, while positive values represent enrichment in the other sample-specific peaks. Graphs show the gene corresponding to each motif, as defined in HOMER's motif table. Statistical analysis was performed with a two-tailed *z*-test, following the calculation of the standard error, with *p*-value adjusted with Bonferroni-Dunn correction, and differences considered statistically significant when adjusted *p*-value < 0.05. For visualization of the accessibility profiles, peaks from replicates were first averaged with WiggleTools (v.1.2)¹⁰² mean, and the resulting wig files were converted to bigwig files with WigtoBigWig (v.3.77)¹⁰³. Principal component analysis (PCA) was performed with deepTools (v.3.5.1)¹⁰⁴, by first computing the average signal for each of the bigwig files before mentioned in all reproducible ATAC-seq peaks

(IDR > 831) with multiBigwigSummary, and then performing and plotting PCA with plotPCA. ATAC-seq heatmaps and profiles were generated with deepTools (v.3.5.1)¹⁰⁴, by first computing a matrix with the parameters “--referencePoint center, -b 500, -a 500, --binSize 10, --sortRegions descend” and the bigwig files abovementioned and by, then, using the tools plotHeatmap and plotProfile, with default parameters. In heatmaps, peaks were ordered by decreasing mean value of ATAC-seq signal per region. To classify the open chromatin regions identified in this study, BEDTools (v.2.29.2) was used to identify the ATAC-seq peaks whose coordinates have some overlap with cCREs derived from ENCODE, using datasets from SCREEN (v.3)²¹.

Correlation between chromatin accessibility of CREs and gene expression

To determine the number of putative CREs in the genomic landscapes of genes whose expression is affected by aging, first, all putative promoters were excluded from further analyses. BEDTools (v.2.29.2) was used to remove ATAC-seq peaks from our datasets that overlapped with any TSS described in Ensembl (v.105), through the BioMart data mining tool^{43,105}. Then, grep -Ff was used to attribute genomic coordinates, also obtained with BioMart, to all differently expressed genes during aging, as determined by RNA-seq and published in Supplementary Data 1 of Macedo and colleagues²⁰ (1435 downregulated and 1860 upregulated). Using Microsoft Excel, the gene start coordinate was extended by 10, 20, 30, 40, and 50 kb in each genomic direction. The resulting coordinates constitute what we define as the genomic landscape of genes, based on genomic distance. To determine the number of putative CREs per gene landscape, the list of ATAC-seq peaks without TSS overlap was crossed with the defined genomic landscapes of differently expressed genes during aging using BEDTools (v.2.29.2) intersect, with option -c. The results were then directly processed and plotted in GraphPad (v8.0.2), with the statistical significance of the differences between the number of ATAC-seq peaks in the landscape of genes downregulated in aging and the number of ATAC-seq peaks in the landscape of genes upregulated in aging determined with the Mann–Whitney test (****p*-value ≤ 0.001, *****p*-value ≤ 0.0001). Error bars represent mean number of ATAC-seq peaks per landscape ± SD.

Gene clusters and gene expression covariation

To define sets of genes whose expression may be co-regulated by shared CREs, all differently expressed genes between neonatal and elderly HDFs (logFC ≥ 0.5; *p*-value ≤ 0.05), as determined by RNA-seq and published in Supplementary Data 1 of Macedo and colleagues²⁰, were selected. Using grep -Ff, transcription start sites (TSS), from a list of TSS obtained from the Ensembl website (v.105), through the BioMart data mining tool^{43,105}, were attributed to all differently expressed genes (1435 downregulated and 1860 upregulated). Those genes were grouped with BEDTools cluster, option -d, so that grouping occurred when TSS are no more than 100,000 bp apart. Using Microsoft Excel, the number of genes showing covariation, either down or upregulation, during aging per cluster was assessed, which was then compared to the expected number, assuming no co-regulation, with a Chi-squared test.

4C-seq (circular chromatin conformation capture followed by next-generation sequencing)

4C-seq was performed on about 10 million cells using the enzymes *DpnII* (first digestion) and *Csp6I* (second digestion), according to van de Werken and colleagues¹⁰⁶ with minor modifications. The 4C template was purified using an Amicon Ultra-15 Centrifugal Filter Device (Milipore). At least two libraries were independently prepared with the Expand Long Template polymerase (Roche) using the primers listed in Supplementary Table 1. Libraries were purified with the QIAquick PCR Purification

kit (QIAGEN) followed by the Agencourt AMPure XP reagent (Beckman Coulter). Libraries were sequenced on HiSeq 2500 system, Rapid Run mode, 1 × 50 bp single-end, at Macrogen. Sequencing data were first inspected for quality control using FASTQC (v.0.11.5)⁹¹ and demultiplexed using the script demultiplex.py from the FourCSeq package¹⁰⁷, allowing for 1 mismatch in the primer sequence. More than 1.5 million reads per sample were aligned to the human genome (hg38) using Bowtie (v1.1.2)¹⁰⁸ (requiring unique alignments, -m 1). Restriction enzyme sites (*DpnII* - GATC and *Csp6I* - GTAC) were mapped on the human genome using Bowtie¹⁰⁸. Fragments flanked by those restriction sites were generated and filtered for size, keeping fragments >40 bp. BEDtools⁹⁹ was used to count sequencing reads within those fragments, generating bedfiles with valid reads counts^{109,110}. Read counts were then smoothed using a 30 bp window average across fragments, generating bedGraph files. For visualization, the smoothed reads from each sample were normalized to 1 million reads per kilobase (https://github.com/porchard/normalize_bedgraph).

Luciferase assays

Putative enhancer sequences and putative promoter sequences were defined based on our ATAC-seq signal and ChIP-seq data (TF clusters and H3K27ac) from the ENCODE project. Sequences were amplified with iMax-II DNA Polymerase (INTRON) from genomic DNA of neonatal HDFs (DFM021711A). Primers used are listed in Supplementary Table 2. Putative enhancer sequences were TA cloned into pCR8/GW/TOPO vector (Invitrogen) and subcloned into pGL4.23-GW¹¹¹ (Addgene #60323) using Gateway LR Clonase II (Gateway cloning, Invitrogen). The empty pGL4.23-GW was used as negative control. The TK promoter from pGL4.54[luc2_TK] (Promega #E5061) was cut with *KpnI* and *HindIII*, ligated into the *KpnI*/*HindIII*-digested pME-MCS¹¹² (To2 kit #237) and subcloned into pGL4.23-GW as above. pNL1.IPGK[Nluc/PGK] (Promega #N1441) was used as transfection control. Cells were transfected in a 6-well plate with 1 pmol of pGL4.23-GW and 0.61 fmol of pNL1.IPGK[Nluc/PGK] per well with Lipofectamine 3000 (Invitrogen) according to manufacturer's instruction. Cells were seeded 12–24 h before transfection. Luciferase activity was assessed 48 h post-transfection using the Nano-Glo Dual-Luciferase Reporter Assay System (Promega) in a Synergy 2 Multi-Mode Microplate Reader (BioTek). The enhancer activity is expressed as the luc2/Nluc ratio (pGL4.23-GW/pNL1.IPGK[Nluc/PGK]), and is presented as a relative response ratio, in which the activity of the empty vector and positive control vector were normalized to 0 and 1, respectively. The enhancer activity of putative enhancers was compared to the control with a one-way analysis of variance (ANOVA) with Dunnett's correction for multiple comparisons (***p*-value ≤ 0.01, *****p*-value ≤ 0.0001), in GraphPad Prism 8.

To test the response of the *JUN*, *ATF3* and *FOS* gene promoter sequences to siRNA against *FOXMI*, the *PGK* promoter from pNL1.IPGK[Nluc/PGK] (Promega #N1441) was removed by digestion with *KpnI* and *HindIII*, and the purified plasmid backbone was used for Gibson cloning. The pGL4.54[luc2_TK] (Promega #E5061) was used as transfection control. pNL1.IPGK[Nluc/PGK] was used as positive control. A multiple-cloning site was inserted in the *KpnI*/*HindIII*-digested pNL1.IPGK[Nluc/PGK], recreating the empty vector pNL1.I[Nluc], which was used as negative control. Putative promoter sequences were selected based on the Eukaryotic Promoter Database EPD¹¹³ and our ATAC-seq data. Sequences were amplified with iMax-II DNA Polymerase (INTRON) from genomic DNA of neonatal HDFs (DFM021711A) and Gibson-cloned into the *KpnI*/*HindIII*-digested pNL1.IPGK[Nluc/PGK]. Primers used are listed in Supplementary Table 3. Cells were seeded in a 24-well plate 12–24 h before transfection. Cells were transfected with 50 nM of a siRNA against *FOXMI* (SASI_Hs01_00243977, Sigma-Aldrich; CAACUCUUCUCCUCAGAU) or a negative control siRNA (siRNA Universal Negative Control #1,

Sigma-Aldrich), using Lipofectamine RNAiMax (Invitrogen), following the manufacturer's instructions. About 24 h later, cells were transfected with 0.5 pmol of pGL4.54[luc2_TK] and 0.05 pmol of the promoter-test vectors per well with Lipofectamine 3000 (Invitrogen). Luciferase activity was assessed 48 h post-transfection (72 h post siRNA transfection) using the Nano-Glo Dual-Luciferase Reporter Assay System (Promega) in a Synergy 2 Multi-Mode Microplate Reader (BioTek). The promoter activity is expressed as a normalized Nluc/luc2 ratio (pNL1.1API[Nluc/API]/pGL4.54[luc2_TK]), in which the ratio of each promoter in cells treated with the control siRNA was normalized to 1, in each independent experiment. The conditions were compared with an unpaired Student's *t*-test using GraphPad Prism 8 (**p*-value ≤ 0.05, ***p*-value ≤ 0.01, ****p*-value ≤ 0.001, *****p*-value ≤ 0.0001). Error bars represent mean ± SD.

CRISPR/Cas9-mediated deletions and FACS-sorting

sgRNA spacer sequences upstream and downstream of the target regions were selected on Benchling¹¹⁴ based on metrics from Doench and colleagues¹¹⁵ and Hsu and colleagues¹¹⁶. Two pairs of sgRNA sequences (each pair targeting one sequence upstream and another sequence downstream the target enhancer) were designed and used independently. The oligonucleotide sequences can be found in Supplementary Table 4. Pairs of oligonucleotides were ordered (Sigma-Aldrich) and annealed, followed by cloning in the *Bbs*I-digested pSpCas9(BB)-2A-GFP (PX458) (Addgene, #48138) and the pU6-(BbsI)_CBh-Cas9-T2A-mCherry (Addgene, #64324) vectors. Neonatal, 1-year-old and 10-year-old HDFs were seeded in 6-well plates and transfected with 250–500 ng of each plasmid per well using Lipofectamine 3000 (Invitrogen) according to the manufacturer's instructions. After 72 h, cells were sorted in a FACSaria II cell sorter (BD Biosciences) using an 85 μm nozzle and the blue (488 nm) and yellow/green (561 nm) lasers. Cells were gated by forward scatter area (FSC-A) vs. side scatter area (SSA-A) and FSC-A vs. FSC-height (FCS-H) plots to exclude dead cells and doublets/clumps, respectively. The gates were established based on the autofluorescence of mock controls. 500–2000 GFP and mCherry double-positive cells were collected into 96-well plates to establish polyclonal cell cultures. A similar number of non-transfected (mock) cells and cells transfected with the empty vectors (Cas9) were always sorted, collected, and grown in parallel to the CRISPR/Cas9-targeted cells. When reaching 75%–95% cell confluency, cells were consecutively transferred to a 48-well, 12-well, 6-well plate and ultimately to a T25 flask, from which cells were used for DNA extraction and genotyping, RNA extraction and RT-qPCR analysis, immunostaining assays, SA-β-gal activity assay and live-cell imaging.

Genotyping

CRISPR/Cas9-mediated genomic deletions were validated in the cultures used for the phenotypic analyses described below. Resuspended cells were washed with 10 mM Tris-HCl pH 8, incubated in Tris buffer at 99 °C for 15 min, and treated with 1 μg/μL proteinase K at 56 °C for 30 min, followed by proteinase K inactivation at 95 °C for 10 min. The extracted DNA was used for genotyping with iMax-II DNA Polymerase (INTRON) following the manufacturer's instructions and adjusting the extension time for each locus. Mock cells and cells transfected with the empty vectors were genotyped in parallel. Primers used are listed in Supplementary Table 5. Efficient deletion of the different loci was determined by the presence of an amplicon with the expected size with a TAE agarose gel, as shown in Supplementary Fig. 4b. Deletion of C10-P2 was further confirmed by Sanger sequencing, as shown in Supplementary Fig. 4c.

Real-time quantitative PCR

Total RNA was extracted using TRIzol reagent (Invitrogen), treated with DNase I (Thermo Scientific), and precipitated with sodium acetate in ethanol. iScript Synthesis Kit (Bio-Rad) was used for cDNA synthesis.

RT-qPCR was performed with iTaq Universal SYBR Green Supermix (Bio-Rad) in a CFX96 or a CFX384 Touch Real-Time PCR Detection System (Bio-Rad) according to the manufacturer's instructions. Primers used are listed in Supplementary Table 6. Data were analyzed using the CFX Maestro software (Bio-Rad). Non-reverse transcribed and blank controls were included. Three technical replicates were used per target gene. Expression was normalized to the *TBP* and *HPRT1* housekeeping genes, and different experimental samples were normalized to the mean expression of the control samples. The samples were compared with an unpaired Student's *t* test using GraphPad Prism 8 (**p*-value ≤ 0.05, ***p*-value ≤ 0.01, ****p*-value ≤ 0.001, *****p*-value ≤ 0.0001).

Immunostaining

Cells were seeded 2–3 days before fixation in 8-well μ-slides (Ibidi) or 96-well CellCarrier Ultra microplates (PerkinElmer). When at 75–95% confluency, were fixed in 4% paraformaldehyde (Electron Microscopy Sciences) in PBS for 15 min, permeabilized with 0.3% Triton-X100 in PBS for 7 min, washed 3 times in 0.05% Tween 20 in PBS (PBS-T) for 5 min, blocked in 10% fetal bovine serum (FBS) in PBS-T for 1 h at RT and incubated with primary antibodies in 5% FBS in PBS-T, overnight at 4 °C. The primary antibodies used in this study were anti-Ki67 (8D5, #9449, Cell Signaling, at 1:500), anti-53BP1 (#4937, Cell Signaling, at 1:500), anti-p21 (F-5, sc-6246, Santa Cruz, 1:800) and anti-p16INK4a (ab7962, Abcam, at 1:200). After washing 3 times in 0.05% Tween 20 in PBS (PBS-T) for 5 min, cells were incubated with secondary antibodies in 5% FBS in PBS-T, at 1:1500, for 45 min at RT. The secondary antibodies used in this study were anti-rabbit Alexa 488 and anti-mouse Alexa 568 (Life Technologies). Samples were then washed 5 times in PBS-T for 5 min, counterstained with DAPI (Sigma-Aldrich, at 1:1000) for 10 min at RT and washed in PBS for 5 min. Images were acquired in a Leica DMI6000 B (Leica Microsystems) equipped with a Hamamatsu FLASH4.0 (Hamamatsu) camera. Images were then analyzed using Fiji – ImageJ (v1.52p, Java 1.8.0)¹¹⁷. Each data point in the graphs corresponds to an independent polyclonal population, of which 500–1200 cells were quantified. The samples were compared by unpaired Student's *t* test using GraphPad Prism 8 (**p*-value ≤ 0.05, ***p*-value ≤ 0.01, ****p*-value ≤ 0.001, *****p*-value ≤ 0.0001).

SA-β-gal activity assay

Cells were seeded 3 days before the assay. Cells were incubated with 100 nM Bafilomycin A1 (Sigma-Aldrich) for 90 min, to induce lysosomal alkalization. The fluorogenic substrate for β-galactosidase, DDAOG (Setareh Biotech), was then added to the cell culture to a final concentration of 10 μM and cells were incubated for 90 min. Cells were then analyzed in a flow cytometry system, namely the FACSaria II cell sorter (BD Biosciences) using an 85 μm nozzle and the red (633 nm) laser. All cells within an experiment were detected using the same voltage settings. Cells were gated by forward scatter area (FSC-A) vs. side scatter area (SSA-A) and FSC-A vs. FSC-height (FCS-H) plots to exclude dead cells and doublets/clumps, respectively. The gates were established based on the autofluorescence of non-treated cells. Around 30000–100000 singlets were analyzed per sample. Analysis of FACS data was done using FlowJo v10 software (FlowJo, LLC). The samples were compared by unpaired Student's *t*-test using GraphPad Prism 8 (**p*-value ≤ 0.05, ***p*-value ≤ 0.01, ****p*-value ≤ 0.001, *****p*-value ≤ 0.0001).

Time-lapse live-cell imaging

Cells were seeded 24 h before image acquisition in 4-well or 8-well μ-slides (Ibidi). Cells were kept under controlled temperature, CO₂ and humidity levels during the experiments and were at 50–75% confluency when imaged. Image acquisition took 6–12 h and each field was imaged every 2.5–4 min. Time-lapse images were either acquired in a Leica DMI6000 B (Leica Microsystems) or in a Nikon TI (Nikon) inverted

microscope, equipped with the cameras Hamamatsu FLASH4.0 (Hamamatsu) or Andor iXon 888 (Andor), respectively. Images were then analyzed using Fiji – ImageJ (v1.52p, Java 1.8.0)¹¹⁷. Mitotic duration was determined as the time (min) from nuclear envelop breakdown (NEB) to anaphase onset (AO). The populations were compared by unpaired Student's *t*-test using GraphPad Prism 8 (**p*-value ≤ 0.05, *****p*-value ≤ 0.0001).

Statistical analysis

Details about statistical analysis and software used can be found in figure legends and respective method descriptions. Values represent mean ± SD. Statistical analysis was performed with GraphPad Prism 8. Regardless of the statistical test, the statistical significance threshold is represented as follows: **p*-value ≤ 0.05, ***p*-value ≤ 0.01, ****p*-value ≤ 0.001, *****p*-value ≤ 0.0001. Exact *p*-values and *n* for all analysis are provided in the Supplementary Data file and/or the Source Data file.

Reporting summary

Further information on research design is available in the Nature Portfolio Reporting Summary linked to this article.

Data availability

The ATAC-seq and 4C-seq sequencing data, as well as the ATAC-seq peaks, generated in this study have been deposited in the European Nucleotide Archive (ENA) at EMBL-EBI under the accession number [PRJEB46917](#). The accession number and description of each dataset are available in the Reporting Summary file. Other previously published ATAC-seq data reanalyzed in this study are available at EMBL-EBI under the accession number [PRJNA439280](#), particularly runs SRR6870410, SRR6870411, SRR6870428, SRR6870432, SRR6870433 and SRR6870434. Source data are provided with this paper.

References

- López-Otín, C., Blasco, M. A., Partridge, L., Serrano, M. & Kroemer, G. Hallmarks of aging: an expanding universe. *Cell* **186**, 243–278 (2023).
- Huang, W., Hickson, L. J., Eirin, A., Kirkland, J. L. & Lerman, L. O. Cellular senescence: the good, the bad and the unknown. *Nat. Rev. Nephrol.* **18**, 611–627 (2022).
- van Deursen, J. M. The role of senescent cells in ageing. *Nature* **509**, 439–446 (2014).
- Hernandez-Segura, A. et al. Unmasking transcriptional heterogeneity in senescent cells. *Curr. Biol.* **27**, 2652–2660.e4 (2017).
- Gill, D. et al. Multi-omic rejuvenation of human cells by maturation phase transient reprogramming. *Elife* **11** (2022).
- Sarkar, T. J. et al. Transient non-integrative expression of nuclear reprogramming factors promotes multifaceted amelioration of aging in human cells. *Nat. Commun.* **11**, 1545 (2020).
- Horvath, S. DNA methylation age of human tissues and cell types. *Genome Biol.* **14**, R115 (2013).
- Cheung, P. et al. Single-cell chromatin modification profiling reveals increased epigenetic variations with aging. *Cell* **173**, 1385–1397.e14 (2018).
- Zhou, X., Sen, I., Lin, X.-X. & Riedel, C. G. Regulation of age-related decline by transcription factors and their crosstalk with the epigenome. *Curr. Genomics* **19**, 464 (2018).
- Bozukova, M. et al. Aging is associated with increased chromatin accessibility and reduced polymerase pausing in liver. *Mol. Syst. Biol.* **18** (2022).
- Itokawa, N. et al. Epigenetic traits inscribed in chromatin accessibility in aged hematopoietic stem cells. *Nat. Commun.* **13**, 2691 (2022).
- Zhang, Y. et al. Single-cell epigenome analysis reveals age-associated decay of heterochromatin domains in excitatory neurons in the mouse brain. *Cell Res.* **32**, 1008–1021 (2022).
- Zaret, K. S. Pioneer transcription factors initiating gene network changes. *Annu. Rev. Genet.* **54**, 367–385 (2020).
- Martínez-Zamudio, R. I. et al. AP-1 imprints a reversible transcriptional programme of senescent cells. *Nat. Cell Biol.* **22**, 842–855 (2020).
- Zhang, C. et al. ATF3 drives senescence by reconstructing accessible chromatin profiles. *Aging Cell* **20**, e13315 (2021).
- Di Giorgio, E. et al. HDAC4 degradation during senescence unleashes an epigenetic program driven by AP-1/p300 at selected enhancers and super-enhancers. *Genome Biol.* **22**, 1–25 (2021).
- Wang, Y., Liu, L., Song, Y., Yu, X. & Deng, H. Unveiling E2F4, TEAD1 and AP-1 as regulatory transcription factors of the replicative senescence program by multi-omics analysis. *Protein Cell* **13**, 742–759 (2022).
- Buenrostro, J. D., Giresi, P. G., Zaba, L. C., Chang, H. Y. & Greenleaf, W. J. Transposition of native chromatin for fast and sensitive epigenomic profiling of open chromatin, DNA-binding proteins and nucleosome position. *Nat. Methods* **10**, 1213–1218 (2013).
- Ma, S., Meng, Z., Chen, R. & Guan, K.-L. The hippo pathway: biology and pathophysiology. *Annu. Rev. Biochem.* **88**, 577–604 (2019).
- Macedo, J. C. et al. FoxM1 repression during human aging leads to mitotic decline and aneuploidy-driven full senescence. *Nat. Commun.* **9**, 1–17 (2018).
- Moore, J. E. et al. Expanded encyclopaedias of DNA elements in the human and mouse genomes. *Nature* **583**, 699–710 (2020).
- Xie, Q. et al. YAP/TEAD-mediated transcription controls cellular senescence. *Cancer Res.* **73**, 3615–3624 (2013).
- Ribeiro, R. et al. In vivo cyclic induction of the FOXM1 transcription factor delays natural and progeroid aging phenotypes and extends healthspan. *Nature Aging* **2**, 397–411 (2022).
- Morris, B. J., Willcox, D. C., Donlon, T. A. & Willcox, B. J. FOXO3: a major gene for human longevity—a mini-review. *Gerontology* **61**, 515–525 (2015).
- Kyoung Kim, H. et al. Down-regulation of a forkhead transcription factor, FOXO3a, accelerates cellular senescence in human dermal fibroblasts. *J. Gerontol. A: Biol. Sci. Med. Sci.* **60**, 4–9 (2005).
- Patrick, R. et al. The activity of early-life gene regulatory elements is hijacked in aging through pervasive AP-1-linked chromatin opening. *Cell Metab.* **36**, 1858–1881.e23 (2024).
- Karakaslar, E. O. et al. Transcriptional activation of Jun and Fos members of the AP-1 complex is a conserved signature of immune aging that contributes to inflammaging. *Aging Cell* **22** (2023).
- Aleksander, S. A. et al. The Gene Ontology knowledgebase in 2023. *Genetics* **224** (2023).
- Huang, J., Wu, S., Barrera, J., Matthews, K. & Pan, D. The Hippo signaling pathway coordinately regulates cell proliferation and apoptosis by inactivating Yorkie, the Drosophila homolog of YAP. *Cell* **122**, 421–434 (2005).
- Watt, K. I., Harvey, K. F. & Gregorevic, P. Regulation of tissue growth by the mammalian Hippo signaling pathway. *Front. Physiol.* **8**, 942 (2017).
- Fu, L. et al. Up-regulation of FOXD1 by yap alleviates senescence and osteoarthritis. *PLoS Biol.* **17**, e3000201 (2019).
- Laoukili, J., Stahl, M. & Medema, R. H. FoxM1: At the crossroads of ageing and cancer. *Biochim. Biophys. Acta (BBA)—Rev. Cancer* **1775**, 92–102 (2007).
- Zona, S., Bella, L., Burton, M. J., Nestal de Moraes, G. & Lam, E. W. F. FOXM1: An emerging master regulator of DNA damage response and genotoxic agent resistance. *Biochim. Biophys. Acta Gene Regul. Mech.* **1839**, 1316–1322 (2014).
- Cotta-Ramusino, C. et al. A DNA damage response screen identifies RHINO, a 9-1-1 and topBP1 interacting protein required for ATR signaling. *Science* **332**, 1313–1317 (2011).

35. Hara, K. et al. Structure of the RAD9-RAD1-HUS1 checkpoint clamp bound to RHINO sheds light on the other side of the DNA clamp. *J. Biol. Chem.* **295**, 899–904 (2020).
36. Brambati, A. et al. RHINO directs MMEJ to repair DNA breaks in mitosis. *Science* **381**, 653–660 (2023).
37. Barger, C. J. et al. Co-regulation and function of FOXM1/RHNO1 bidirectional genes in cancer. *Elife* **10** (2021).
38. Nguyen, N. T. T., Vincens, P., Dufayard, J. F., Roest Crolius, H. & Louis, A. Genomicus in 2022: comparative tools for thousands of genomes and reconstructed ancestors. *Nucleic Acids Res.* **50**, D1025–D1031 (2022).
39. Bateman, A. et al. UniProt: the Universal Protein Knowledgebase in 2023. *Nucleic Acids Res.* **51**, D523–D531 (2023).
40. Yu, J. K. et al. The Fox genes of Branchiostoma floridae. *Dev. Genes Evol.* **218**, 629–638 (2008).
41. Aldea, D., Leon, A., Bertrand, S. & Escriva, H. Expression of Fox genes in the cephalochordate Branchiostoma lanceolatum. *Front. Ecol. Evol.* **3**, 80 (2015).
42. Marlétaz, F. et al. Amphioxus functional genomics and the origins of vertebrate gene regulation. *Nature* **564**, 64–70 (2018).
43. Cunningham, F. et al. Ensembl 2022. *Nucleic Acids Res.* **50**, D988–D995 (2022).
44. Lindsey-Boltz, L. A., Kemp, M. G., Capp, C. & Sancar, A. RHINO forms a stoichiometric complex with the 9-1-1 checkpoint clamp and mediates ATR-Chk1 signaling. *Cell Cycle* **14**, 99–108 (2015).
45. Rosenbloom, K. R. et al. ENCODE data in the UCSC Genome Browser: year 5 update. *Nucleic Acids Res.* **41**, D56–D63 (2013).
46. Navarro Gonzalez, J. et al. The UCSC genome browser database: 2021 update. *Nucleic Acids Res.* **49**, D1046–D1057 (2021).
47. Liang, G. et al. Distinct localization of histone H3 acetylation and H3-K4 methylation to the transcription start sites in the human genome. *Proc. Natl Acad. Sci. USA* **101**, 7357–7362 (2004).
48. Du, D. et al. RHNO1 disruption inhibits cell proliferation and induces mitochondrial apoptosis via PI3K/Akt pathway in hepatocellular carcinoma. *Biochem. Biophys. Res. Commun.* **673**, 96–105 (2023).
49. Laoukili, J. et al. FoxM1 is required for execution of the mitotic programme and chromosome stability. *Nat. Cell Biol.* **7**, 126–136 (2005).
50. Kim, J.-W. et al. Involvement of C12orf32 overexpression in breast carcinogenesis. *Int. J. Oncol.* **37** (2010).
51. Takeuchi, S. et al. TEAD4-YAP interaction regulates tumoral growth by controlling cell-cycle arrest at the G1 phase. *Biochem. Biophys. Res. Commun.* **486**, 385–390 (2017).
52. Hazan, I. et al. Activation of oncogenic super-enhancers is coupled with DNA repair by RAD51 article activation of oncogenic super-enhancers is coupled with DNA repair by RAD51. *Cell Rep.* **29**, 560–572 (2019).
53. Laoukili, J., Alvarez-Fernandez, M., Stahl, M. & Medema, R. H. FoxM1 is degraded at mitotic exit in a Cdh1-dependent manner. *Cell Cycle* **7**, 2720–2726 (2008).
54. Laoukili, J. et al. Activation of FoxM1 during G2 requires cyclin A/ Cdk-dependent relief of autorepression by the FoxM1 N-terminal domain. *Mol. Cell Biol.* **28**, 3076–3087 (2008).
55. Shaulian, E. & Karin, M. AP-1 as a regulator of cell life and death. *Nat. Cell Biol.* **4**, E131–E136 (2002).
56. Garcés de Los Fayos Alonso, I. et al. The role of activator protein-1 (AP-1) family members in CD30-positive lymphomas. *Cancers (Basel)* **10** (2018).
57. Sen, P., Shah, P. P., Nativio, R. & Berger, S. L. Epigenetic mechanisms of longevity and aging. *Cell* **166**, 822–839 (2016).
58. Stegeman, R. & Weake, V. M. Transcriptional signatures of aging. *J. Mol. Biol.* **429**, 2427–2437 (2017).
59. Buenrostro, J. D. et al. Single-cell chromatin accessibility reveals principles of regulatory variation. *Nature* **523**, 486–490 (2015).
60. Zheng, H. & Xie, W. The role of 3D genome organization in development and cell differentiation. *Nat. Rev. Mol. Cell Biol.* **20**, 535–550 (2019).
61. Miguel-Escalada, I. et al. Human pancreatic islet three-dimensional chromatin architecture provides insights into the genetics of type 2 diabetes. *Nat. Genet.* **51**, 1137–1148 (2019).
62. Zhu, L., Song, W., Ovcharenko, I. & Landsman, D. A model of active transcription hubs that unifies the roles of active promoters and enhancers. *Nucleic Acids Res.* **49**, 4493–4505 (2021).
63. Sladitschek-Martens, H. L. et al. YAP/TAZ activity in stromal cells prevents ageing by controlling cGAS–STING. *Nature* **607**, 790–798 (2022).
64. Pattschull, G. et al. The Myb-MuvB complex is required for YAP-dependent transcription of mitotic genes. *Cell Rep.* **27**, 3533–3546.e7 (2019).
65. Gründl, M. et al. Interaction of YAP with the Myb-MuvB (MMB) complex defines a transcriptional program to promote the proliferation of cardiomyocytes. *PLoS Genet.* **16** (2020).
66. Wolfson, R. L. et al. KICSTOR recruits GATOR1 to the lysosome and is necessary for nutrients to regulate mTORC1. *Nature* **543**, 438–442 (2017).
67. Palmer, D., Fabris, F., Doherty, A., Freitas, A. A. & de Magalhães, J. P. Ageing transcriptome meta-analysis reveals similarities and differences between key mammalian tissues. *Aging* **13**, 3313–3341 (2021).
68. Devane, J. et al. Progressive liver, kidney, and heart degeneration in children and adults affected by TULP3 mutations. *Am. J. Hum. Genet.* **109**, 928–943 (2022).
69. Chandra, T. et al. Global reorganization of the nuclear landscape in senescent cells. *Cell Rep.* **10**, 471–483 (2015).
70. Zirkel, A. et al. HMGB2 loss upon senescence entry disrupts genomic organization and induces CTCF clustering across cell types. *Mol. Cell* **70**, 730–744.e6 (2018).
71. Guan, Y. et al. Senescence-activated enhancer landscape orchestrates the senescence-associated secretory phenotype in murine fibroblasts. *Nucleic Acids Res.* **48**, 10909–10923 (2020).
72. Moskowitz, D. M. et al. Epigenomics of human CD8 T cell differentiation and aging. *Sci. Immunol.* **2** (2017).
73. Ucar, D. et al. The chromatin accessibility signature of human immune aging stems from CD8+ T cells. *J. Exp. Med.* **214**, 3123–3144 (2017).
74. Shan, X., Roberts, C., Lan, Y. & Percec, I. Age alters chromatin structure and expression of SUMO proteins under stress conditions in human adipose-derived stem cells. *Sci. Rep.* **8**, 11502 (2018).
75. Morandini, F. et al. ATAC-clock: an aging clock based on chromatin accessibility. *Geroscience* **46**, 1789–1806 (2024).
76. Han, R. et al. Functional CRISPR screen identifies AP1-associated enhancer regulating FOXF1 to modulate oncogene-induced senescence. *Genome Biol.* **19**, 1–13 (2018).
77. Li, K. et al. Interrogation of enhancer function by enhancer-targeting CRISPR epigenetic editing. *Nat. Commun.* **11**, 1–16 (2020).
78. Torigoe, T. H. et al. Novel protective effect of the FOXO3 longevity genotype on mechanisms of cellular aging in Okinawans. *npj Aging* **10**, 18 (2024).
79. Zou, H. et al. Tyrosine phosphorylation-mediated YAP1-TFAP2A interactions coordinate transcription and trastuzumab resistance in HER2+ breast cancer. *Drug Resistance Updates* **73**, 101051 (2024).
80. Zhu, M. et al. Tead4 and Tfap2c generate bipotency and a bistable switch in totipotent embryos to promote robust lineage diversification. *Nat. Struct. Mol. Biol.* **31**, 964–976 (2024).

81. Šošić, D., Richardson, J. A., Yu, K., Ornitz, D. M. & Olson, E. N. Twist regulates cytokine gene expression through a negative feedback loop that represses NF- κ B Activity. *Cell* **112**, 169–180 (2003).
82. Kim, J. Y. et al. Twist2-driven chromatin remodeling governs the postnatal maturation of dermal fibroblasts. *Cell Rep.* **39**, 110821 (2022).
83. Nguyen, H. et al. Tcf3 and Tcf4 are essential for long-term homeostasis of skin epithelia. *Nat. Genet.* **41**, 1068–1075 (2009).
84. Maity, P. et al. Persistent JunB activation in fibroblasts disrupts stem cell niche interactions enforcing skin aging. *Cell Rep.* **36**, 109634 (2021).
85. Hou, Y. et al. CTCF mediates replicative senescence through POLD1. *Front. Cell Dev. Biol.* **9**, 164 (2021).
86. Shen, X. et al. Nonlinear dynamics of multi-omics profiles during human aging. *Nat. Aging* **4**, 1619–1634 (2024).
87. Bai, H. et al. Progressive senescence programs induce intrinsic vulnerability to aging-related female breast cancer. *Nat. Commun.* **15**, 5154 (2024).
88. Kumaki, Y., Oda, M. & Okano, M. QUMA: quantification tool for methylation analysis. *Nucleic Acids Res.* **36** (2008).
89. Buenrostro, J. D., Wu, B., Chang, H. Y. & Greenleaf, W. J. ATAC-seq: a method for assaying chromatin accessibility genome-wide. *Curr. Protoc. Mol. Biol.* **2015**, 21.29.1–21.29.9 (2015).
90. Picelli, S. et al. Tn5 transposase and tagmentation procedures for massively scaled sequencing projects. *Genome Res.* **24**, 2033–2040 (2014).
91. Andrews, S. FastQC: a quality control tool for high throughput sequence data [Online]. Available at <http://www.bioinformatics.babraham.ac.uk/projects/fastqc/> (2010).
92. Jiang, H., Lei, R., Ding, S. W. & Zhu, S. Skewer: A fast and accurate adapter trimmer for next-generation sequencing paired-end reads. *BMC Bioinformatics* **15** (2014).
93. Chen, S., Zhou, Y., Chen, Y. & Gu, J. fastp: an ultra-fast all-in-one FASTQ preprocessor. *Bioinformatics* **34**, i884–i890 (2018).
94. Langmead, B. & Salzberg, S. L. Fast gapped-read alignment with Bowtie 2. *Nat. Methods* **9**, 357–359 (2012).
95. Li, H. et al. The Sequence Alignment/Map format and SAMtools. *Bioinformatics* **25**, 2078–2079 (2009).
96. Zhang, Y. et al. Model-based analysis of ChIP-Seq (MACS). *Genome Biol* **9** (2008).
97. Li, Q., Brown, J. B., Huang, H. & Bickel, P. J. Measuring reproducibility of high-throughput experiments. *Ann. Appl. Stat.* **5**, 1752–1779 (2011).
98. Amemiya, H. M., Kundaje, A. & Boyle, A. P. The ENCODE blacklist: identification of problematic regions of the genome. *Sci. Rep.* **9**, 1–5 (2019).
99. Quinlan, A. R. & Hall, I. M. BEDTools: a flexible suite of utilities for comparing genomic features. *Bioinformatics* **26**, 841–842 (2010).
100. Love, M. I., Huber, W. & Anders, S. Moderated estimation of fold change and dispersion for RNA-seq data with DESeq2. *Genome Biol.* **15**, 1–21 (2014).
101. Heinz, S. et al. Simple combinations of lineage-determining transcription factors prime cis-regulatory elements required for macrophage and B cell identities. *Mol. Cell* **38**, 576–589 (2010).
102. Zerbino, D. R., Johnson, N., Juettemann, T., Wilder, S. P. & Flicek, P. WiggleTools: parallel processing of large collections of genome-wide datasets for visualization and statistical analysis. *Bioinformatics* **30**, 1008–1009 (2014).
103. Kent, W. J., Zweig, A. S., Barber, G., Hinrichs, A. S. & Karolchik, D. BigWig and BigBed: enabling browsing of large distributed datasets. *Bioinformatics* **26**, 2204–2207 (2010).
104. Ramírez, F. et al. deepTools2: a next generation web server for deep-sequencing data analysis. *Nucleic Acids Res.* **44**, W160–W165 (2016).
105. Kinsella, R. J. et al. Ensembl BioMart: a hub for data retrieval across taxonomic space. *Database* **2011** (2011).
106. van de Werken, H. J. G. et al. in *Methods in Enzymology* vol. 513 89–112 (Academic Press Inc., 2012).
107. Klein, F. A. et al. FourCSeq: analysis of 4C sequencing data. *Bioinformatics* **31**, 3085–3091 (2015).
108. Langmead, B., Trapnell, C., Pop, M. & Salzberg, S. L. Ultrafast and memory-efficient alignment of short DNA sequences to the human genome. *Genome Biol.* **10** (2009).
109. Noordermeer, D. et al. The dynamic architecture of Hox gene clusters. *Science* **334**, 222–225 (2011).
110. Splinter, E., de Wit, E., van de Werken, H. J. G., Klous, P. & de Laat, W. Determining long-range chromatin interactions for selected genomic sites using 4C-seq technology: From fixation to computation. *Methods* **58**, 221–230 (2012).
111. Pasquali, L. et al. Pancreatic islet enhancer clusters enriched in type 2 diabetes risk-associated variants. *Nat. Genet.* **46**, 136–143 (2014).
112. Kwan, K. M. et al. The Tol2kit: A multisite gateway-based construction Kit for Tol2 transposon transgenesis constructs. *Dev. Dyn.* **236**, 3088–3099 (2007).
113. Dreos, R., Ambrosini, G., Groux, R., Perier, R. C. & Bucher, P. The eukaryotic promoter database in its 30th year: focus on non-vertebrate organisms. *Nucleic Acids Res.* **45**, D51–D55 (2017).
114. Benchling [Biology Software]. Retrieved from <https://benchling.com> (2018).
115. Doench, J. G. et al. Optimized sgRNA design to maximize activity and minimize off-target effects of CRISPR-Cas9. *Nat. Biotechnol.* **34**, 184–191 (2016).
116. Hsu, P. D. et al. DNA targeting specificity of RNA-guided Cas9 nucleases. *Nat. Biotechnol.* **31**, 827–832 (2013).
117. Schindelin, J. et al. Fiji: an open-source platform for biological-image analysis. *Nat. Methods* **9**, 676–682 (2012).

Acknowledgements

The authors thank Juan Tena (CABD, CSIC-UPO, Seville) for kindly sharing custom scripts for 4C-seq data processing; Vincent Macaulay (School of Mathematics and Statistics, University of Glasgow) for his time, useful discussion and suggestions regarding statistical analysis of motif enrichment; and i3S Scientific Platforms: BioSciences Screening; Translational Cytometry; Cell Culture and Genotyping; Genomics; and Advanced Light Microscopy, member of PPBI (POCI-01-0145-FEDER-022122) for their technical support. The following grants supported this work: European Research Council (ERC) under the European Union's Horizon 2020 research and innovation program (ERC-2015-StG-680156-ZPR); "La Caixa" Foundation (under the grant agreement HR21-01212); and Fundação para a Ciência e a Tecnologia (FCT) in the framework of the project PTDC/BIA-MOL/3834/2021 to J.B. Maximon Longevity Prize 2022 (Maximon AG, Switzerland); FCT in the framework of the project PTDC/MED-OUT/2747/2020; FEDER (Fundo Europeu de Desenvolvimento Regional) through the COM-PETE 2020—Operational Programme for Competitiveness and Internationalization (POCI), Portugal 2020, and in the framework of the project POCI-01-0145-FEDER-031120 (PTDC/BIA-CEL/31120/2017) to E.L. COMPETE 2020/ PORTUGAL 2020 through FEDER, for project POCI-01-0145-FEDER-007274 in the i3S framework, to J.B. and E.L. FCT grants CEECIND/03482/2018 and CEECIND/00654/2020 to J.B. and E.L., respectively. FCT PhD fellowships PD/BD/105745/2014 and SFRH/BD/126467/2016 to F.J.F. and J.T., respectively. The funders had no role in study design, data collection and analysis, decision to publish or preparation of the manuscript.

Author contributions

F.J.F. performed all wet lab experiments and respective analyses. F.J.F. and M.G. performed computational analyses and data

interpretation. J.M.N. performed genotyping of cells following CRISPR/Cas9-mediated genomic editing. J.T. performed preliminary ATAC-seq plotting. J.B. and E.L. supervised the project and contributed to all analyses. F.J.F., J.B., and E.L. conceptualized the work, designed experiments and wrote the manuscript with input from all authors. All authors read and agreed to the final version of the manuscript.

Competing interests

The authors declare no competing interests.

Additional information

Supplementary information The online version contains supplementary material available at <https://doi.org/10.1038/s41467-025-57503-4>.

Correspondence and requests for materials should be addressed to Elsa Logarinho or José. Bessa.

Peer review information *Nature Communications* thanks Yu Sun, and the other, anonymous, reviewer(s) for their contribution to the peer review of this work. A peer review file is available.

Reprints and permissions information is available at <http://www.nature.com/reprints>

Publisher's note Springer Nature remains neutral with regard to jurisdictional claims in published maps and institutional affiliations.

Open Access This article is licensed under a Creative Commons Attribution-NonCommercial-NoDerivatives 4.0 International License, which permits any non-commercial use, sharing, distribution and reproduction in any medium or format, as long as you give appropriate credit to the original author(s) and the source, provide a link to the Creative Commons licence, and indicate if you modified the licensed material. You do not have permission under this licence to share adapted material derived from this article or parts of it. The images or other third party material in this article are included in the article's Creative Commons licence, unless indicated otherwise in a credit line to the material. If material is not included in the article's Creative Commons licence and your intended use is not permitted by statutory regulation or exceeds the permitted use, you will need to obtain permission directly from the copyright holder. To view a copy of this licence, visit <http://creativecommons.org/licenses/by-nc-nd/4.0/>.

© The Author(s) 2025